Coastal Engineering 209 (2026) 105039

Contents lists available at ScienceDirect

Coastal Engineering

journal homepage: www.elsevier.com/locate/coastaleng

Wave overtopping discharges at rubble mound structures in shallow water: Effects of directional spreading

Menno P. de Ridder [a,b,*], Dennis C.P. van Kester [c,b], Patricia Mares-Nasarre [b], Marcel R.A. van Gent [a,b]

[a] Deltares, Department of Coastal Structures and Waves, The Netherlands
[b] Delft University of Technology, Department of Hydraulic Engineering, Delft, The Netherlands
[c] Van Oord, Rotterdam, The Netherlands

ARTICLE INFO

Dataset link: https://deltares-coastal-structures-toolbox.readthedocs.io/en/stable/

Keywords:
Wave overtopping
Shallow foreshore
Rubble mound breakwater
Coastal structures
Low-frequency energy
Physical model tests
Directional spreading

ABSTRACT

Physical model experiments are conducted in a wave basin to investigate the influence of directional spreading on wave overtopping in shallow water. Offshore wave steepness, wave height, water depth, and directional spreading are systematically varied to assess their impact on the non-dimensional mean overtopping discharge (q^*). Additional tests with oblique wave attack are performed to examine the role of the wave direction.

To better understand the underlying hydrodynamics, the dependence of low-frequency wave energy on directional spreading is analyzed. Results confirm that low-frequency wave energy strongly depends on directional spreading, consistent with previous studies. An empirical formulation is introduced to predict the ratio of low-frequency wave height to total incident wave height using the relative water depth, the offshore wave steepness, and offshore directional spreading, achieving an $R^2 = 0.91$. Excluding directional spreading from the formulation decreases the R^2 to 0.38, highlighting its importance.

Variations in low-frequency wave energy also affect q^*, as low-frequency waves temporarily raise the water level, leading to larger overtopping volumes and thus higher q^*. Consequently, directional spreading influences q^* primarily through its effect on low-frequency energy, particularly in shallow water.

To evaluate how existing prediction tools perform under these conditions, several formulations for q^* are assessed. Their performance ranges from poor to reasonable, with the best results using the formulation in De Ridder et al. (2024) that were based on 2DV tests in shallow water rather than 3D tests including directional spreading. The tests with oblique waves show that the existing formulation captures the trends found in shallow water. Therefore, the existing formulation for the influence of oblique wave attack is also recommended for shallow water.

To incorporate directional spreading effects into overtopping prediction, the relative crest height was adjusted by including the contribution of the low-frequency wave height as done in De Ridder et al. (2024). Due to reduced correlation between the short-wave steepness and the low-frequency height in this new dataset, coefficients could be estimated more reliably. The revised equations are validated against (long-crested) wave flume and new datasets with both short- and long-crested conditions and oblique attack. The expression including the low-frequency wave height results in the highest accuracy ($R^2 = 0.87$, Equation (32)) and is recommended, while a relatively simple expression with only the relative crest and short-wave steepness also performs well ($R^2 = 0.83$, Equation (28)).

1. Introduction

Coastal structures have a critical role in coastal regions to prevent the hinterland from flooding or protect ports and recreational areas. Therefore, it is important to efficiently design these structures to withstand extreme wave conditions, especially in the context of climate change. One of the key design parameters to determine the freeboard (R_c) is the mean overtopping discharge (q).

To address growing uncertainty in wave conditions and sea level rise, climate-adaptive strategies are gaining attention (e.g. Van Gent, 2019; Van Gent and Teng, 2023). Rather than incorporating all uncertainties into the initial design, these strategies allow for adjustments

* Corresponding author at: Deltares, Department of Coastal Structures and Waves, The Netherlands.
E-mail address: menno.deridder@deltares.nl (M.P. de Ridder).

https://doi.org/10.1016/j.coastaleng.2026.105039
Received 4 February 2026; Received in revised form 3 April 2026; Accepted 20 April 2026
Available online 2 May 2026

of the structure when the conditions require it. One of such measures is a shallow foreshore by sand nourishment in front of the structure to reduce the wave loading on the structure. Thus, it is necessary to understand how the processes at a shallow foreshore affect wave overtopping.

Previous studies have examined the relationship between wave overtopping, wave characteristics, and structural properties (e.g. structure slope and roughness). Based on the pioneering work of Owen (1980) and Battjes (1972), a formula was derived to estimate the non-dimensional wave overtopping discharge q^*, which is the basis of the current guidelines (e.g. TAW, 2002; EurOtop, 2018; Van Gent et al., 2025). Several studies have developed formulations for shallow water conditions (e.g. Van Gent, 1999, 2001; Altomare et al., 2016; Lashley et al., 2021; De Ridder et al., 2024). Recently, physical model experiments for wave overtopping with a shallow foreshore were conducted in a wave flume (De Ridder et al., 2024, 2025), where an empirical formula was proposed based on only near-shore hydrodynamic parameters using the relative crest height ($R_c^*= R_c/H_{m0}$ with R_c the freeboard and H_{m0} the wave height), short-wave steepness ($s_{m-1,0,HF} = 2\pi H_{m0,HF}/(gT^2_{m-1,0,HF})$ with $H_{m0,HF}$ the short-wave height and $T_{m-1,0,HF}$, the short-wave spectral period), and optionally the low-frequency wave height ($H_{m0,LF}$) using a frequency split of $f_p/1.5$. Moreover, it has been shown that these low-frequency waves are an important aspect of the wave overtopping in shallow water (e.g. Lashley et al., 2022; De Ridder et al., 2024). Although, it is known that the low-frequency waves are largely dependent on the directional spreading (e.g. Herbers and Burton, 1997; Klopman and Dingemans, 2001), this effect could not be verified using flume experiments, leading to a formula mainly valid for long-crested wave conditions. Moreover, the $s_{m-1,0,HF}$ and $H_{m0,LF}$ are correlated in the flume experiments as under low-steepness conditions, more energy is transferred to lower frequencies (e.g. De Ridder et al., 2024, 2025). This correlation makes it difficult to isolate the effect of $H_{m0,LF}$ on q^* based on solely flume experiments.

Research on effects of directional spreading (σ_θ) on nearshore wave parameters and especially q^* remains limited. Altomare et al. (2020) investigated the influence of a shallow foreshore (1:35 slope) with variations in σ_θ on q^*, providing a reduction factor for q^*. However, their study did not describe the associated hydrodynamic changes, such as the evolution of low-frequency waves or directional spreading. Field measurements by Guza and Feddersen (2012) showed that directional spreading significantly affects runup through low-frequency oscillations. Numerical studies (e.g. Suzuki et al., 2014) highlighted the role of second-order wave generation and bottom friction, while physical experiments by Nørgaard et al. (2013) found that the direction of overtopping events align with the mean offshore wave direction. Nevertheless, quantitative insight into the effects of directional spreading on nearshore wave variables (e.g., $H_{m0,LF}$) and q^* remains limited.

This study verifies the experimental findings of De Ridder et al. (2024), 2DV thus without directional spreading, for various values of directional spreading using 3D physical model experiments. By systematically varying wave conditions, the influence of directional spreading on both nearshore wave variables and q^* is assessed. Additional tests with oblique waves validate overtopping formulations under shallow water conditions.

The paper is organized as follows: Section 2 provides the background information, Section 3 describes the experimental setup, Sections 4 and 5 present the hydrodynamic and overtopping results, respectively, followed by the derivation of the new formulation in Section 6. Section 7 contains the discussion and conclusions and recommendations are given in Section 8.

2. Background

2.1. Directional spreading

When wind generates waves, the energy is not concentrated in a single direction but distributed across a range of frequencies (f) and wave directions (θ), forming a directional wave field captured by a directional wave spectrum ($E(f,\theta)$). The first measurements of directional wave spectra, obtained using pitch-and-roll buoys, revealed that directional spreading decreases as wind fetch increases (Longuet-Higgins, 1963; Mitsuyasu et al., 1975; Hasselmann et al., 1980). Subsequently, various techniques were developed to estimate directional spectra more accurately (e.g., Isobe and Kondo, 1985; Kuik et al., 1988; Hashimoto et al., 1995). It was also shown that swell-dominated conditions typically exhibit narrower directional spreading because these waves are more organized and propagate over long distances (e.g., Forristall and Ewans, 1998).

Several directional spreading functions have been proposed. A widely used example is the cosine-shaped function introduced by Longuet-Higgins (1963),

$$D(\theta) = \frac{2^{s-1}}{\pi}\frac{\Gamma(s+1)^2}{\Gamma(s+1)}\cos\left(\frac{\theta-\theta_m}{2}\right)^{2s} \tag{1}$$

where $D(\theta)$ is the directional distribution, $\Gamma(...)$ is the gamma function, s represents the spreading (larger s indicates narrower spreading), θ the direction and θ_m the mean direction. The directional spreading (σ_θ) is given by (Eq. 6.3.21 in Holthuijsen, 2007),

$$\sigma_\theta^2 = \int_{-\infty}^{\infty}\left(2\sin(\frac{1}{2}\theta)\right)^2 D(\theta)d\theta \tag{2}$$

where θ is the direction and $D(\theta)$ the direction distribution. Given this distribution, s and σ_θ (in radians) are related by,

$$\sigma_\theta = \sqrt{\frac{2}{s+1}} \tag{3}$$

Typical values for the directional spreading are $s = 6$ for wind sea ($\sigma_\theta \approx 30°$), $s = 60$ ($\sigma_\theta \approx 10°$) for swell conditions. In this study, the wave fields generated are based on Eq. (1).

2.2. Wave overtopping

Several studies have investigated the effect of wave parameters on the q. Based on the pioneering work of Saville (1955), Battjes (1972) and Goda et al. (1975), and the analytical expression for overflow of a weir (Kikkawa et al., 1968), Owen (1980) proposed an exponential function to describe the non-dimensional mean overtopping discharge,

$$q^* = a\exp\left(-b\frac{R^*}{\gamma_f}\right) \tag{4}$$

where q^* is the non-dimensional mean overtopping discharge given by $q/\sqrt{gH_{m0}^3}$ where H_{m0} is the wave height, R_c^* the non-dimensional crest level and γ_f a roughness factor.

This expression was extended by Van der Meer and Janssen (1994) with a maximum value of q, based on similarities between the runup height and the Iribarren number found by Battjes (1974). Later, Van Gent (1999, 2001) proposed using $T_{m-1,0}$ as the characteristic wave period instead of the mean wave period, demonstrating that this parameter enables accurate predictions of wave runup and overtopping across various spectral shapes. These findings resulted in the wave overtopping formulation as given in the (TAW, 2002) manual, which is given by,

$$\frac{q}{\sqrt{gH_{m0}^3}} = 0.067\xi_{m-1,0}\exp\left(-4.74\frac{R_c}{H_{m0}}\frac{1}{\gamma_f\xi_{m-1,0}}\right) \tag{5}$$

with a maximum of

$$\frac{q}{\sqrt{gH_{m0}^3}} = 0.2\exp\left(-2.6\frac{R_c}{H_{m0}}\frac{1}{\gamma_f}\right) \tag{6}$$

where $\xi_{m-1,0}$ is the Iribarren number given by $\frac{\tan(\alpha)}{\sqrt{s_{m-1,0}}}$ where the wave steepness is given by $s_{m-1,0} = 2\pi H_{m0}/(gT^2_{m-1,0})$ and α is the structure slope.

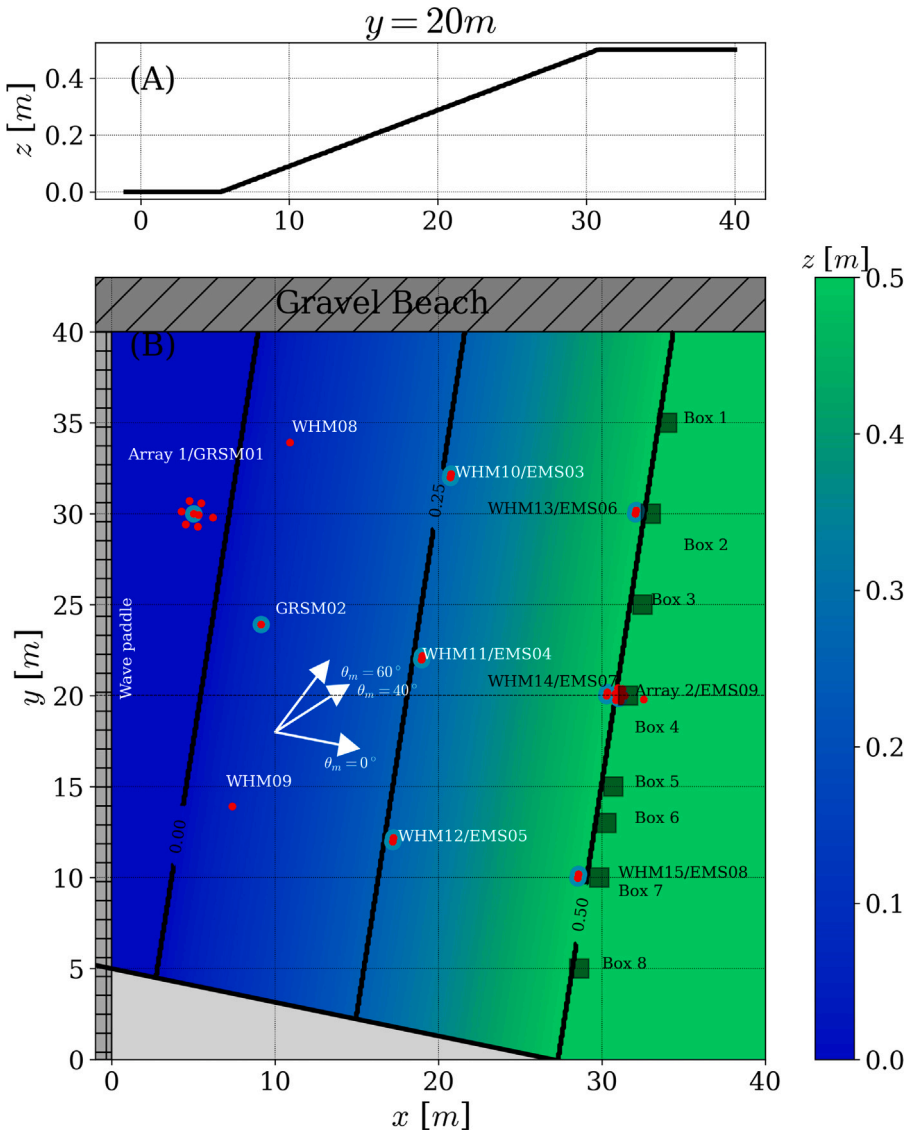

Fig. 1. Overview of the basin showing the instrument locations and bathymetry in Panel B and a cross-section of the floor level at y = 20 m in Panel A. The wave maker is positioned on the left (x = 0 m). Wave gauges are indicated in red, velocity instruments in cyan, and overtopping boxes are represented by gray squares (squares only show location but do not represent the size or rotation of the boxes). z [m] denotes the floor level.

These expressions were mainly derived for relatively deep water. The TAW (2002) manual also provides an expression for shallow water based on Van Gent (1999) given by,

$$\frac{q}{\sqrt{gH_{m0}^3}} = 0.12\exp\left(-\frac{R_c}{H_{m0}\gamma_f(0.33+0.022\xi_{m-1,0})}\right) \tag{7}$$

Since most rubble mound structures have a steep slope for deep water conditions, Eq. (6) normative for such structures, is the main formulation in the EurOtop (2007) for rubble mound breakwaters. This formulation was modified in EurOtop (2018) adding power in the formulation leading to,

$$\frac{q}{\sqrt{gH_{m0}^3}} = 0.09\exp\left(-(1.5\frac{R_c}{H_{m0}\gamma_{f,mod}})^{1.3}\right) \tag{8}$$

Next to the addition of the power in EurOtop (2018), the roughness coefficient was changed for very steep and/or very long waves with $\xi_{m-1,0} > 5$,

$$\gamma_{f,mod} = \gamma_f + \frac{(\xi_{m-1,0}-5)(1-\gamma_f)}{5} \tag{9}$$

These formulas form the basis of the current guidelines for deep and shallow water for rubble mound structures.

For shallow water conditions, in addition to Eq. (7), several alternative formulations have been proposed (Altomare et al., 2016; Lashley et al., 2021; De Ridder et al., 2024). Altomare et al. (2016) modified Eq. (7) by introducing an equivalent slope concept in the breaker parameter (see Appendix A). Lashley et al. (2021) developed a formulation based on deep-water wave conditions and the foreshore slope. More recently, De Ridder et al. (2024) proposed a formulation relying solely on nearshore wave parameters, using R_c^* and incorporating $H_{m0,LF}$ to account for slowly varying water-level fluctuations (see Appendix A). Van Gent et al. (2025) derived an alternative formulation using the $s_{m-1,0}$, α and R_c^*.

The influence of directional spreading on wave overtopping was investigated through physical model experiments by Altomare et al. (2020). Based on these experiments, Altomare et al. (2020) introduced an influence factor to account for σ_θ in the modified Eq. (7) (see Appendix A for the expression), expressed as,

$$\gamma_\sigma = \begin{cases} \exp(-0.046\sigma_{\theta,0}) & \text{for } \frac{h}{H_{m0,deep}} < 0.3 \\ \exp(-0.014\sigma_{\theta,0}) & \text{for } 0.3 < \frac{h}{H_{m0,deep}} < 0.1 \end{cases} \quad (10)$$

with $\sigma_{\theta,0}$ being the offshore directional spreading in degrees, h the local water depth at the toe and $H_{m0,deep}$ the spectral deep water wave height. A similar factor for the effect of directional spreading was expressed for q of Goda (2009) by Altomare et al. (2020). However, these formulations do not explicitly account for the effects of low-frequency waves, which is the main focus of this study.

3. Wave basin tests

3.1. Model set-up

Physical model experiments are conducted in the Delta Basin of Deltares. The layout of the model is shown in Fig. 1. The concrete foreshore has a 1:50 slope up to a height of 0.5 m and is rotated by −10° relative to the wave maker. This rotation increases the wave direction at the toe for tests under oblique wave conditions and helps to reduce potential standing waves in the basin. Tests with and without a structure at the end of the foreshore are performed to obtain reliable incident waves.

At the lower part of the model, a vertical wall perpendicular to the depth contour is present (from $x = 0$ m, $y = 5$ m till $x \approx 25$ m, $y = 0$ m). For tests with normally incident waves, with and without directional spreading, this wall causes reflection, thereby reducing the shadow zone. At the upper end ($y = 40$ m), a gravel beach is located to absorb wave energy, which is particularly relevant for tests with oblique waves. Because this gravel beach is not rotated, a diffraction zone appears in the upper part during tests with normally incident waves. However, this effect is expected to have minimal influence on the overtopping boxes located in the center of the basin. The extent of the diffraction zone was assessed by comparing the results from multiple overtopping boxes (See Section 3.4.1). In addition, a comparison of the measured wave heights shows that the difference between WHM15 and WHM14 is small (mean deviation of 0.0006 m), while a larger difference is observed between WHM14 and WHM13 (0.004 m) for conditions with $\theta_m = 0°$. These findings indicate that the gravel beach does not influence the conditions at WHM14 which is used for the analysis for tests with $\theta_m = 0°$. During the calibration tests (without the structure in place), an absorbing beach is also located at the rear-side of the basin ($x \approx 40$ m) to absorb most of the wave energy.

Free-surface elevation is measured using wave gauges and GRSMs, with the latter also recording velocities. EMSs are employed specifically for velocity measurements. Both EMSs and GRSMs are primarily used to determine the directional wave spectrum, $E(f,\theta)$. The GRSM measures free-surface elevation and velocity at the same location, while EMSs, which measure only velocity, are positioned near a wave gauge (see Table 1). When determining the directional wave spectrum using velocities and free surface elevations, these small spatial differences between instruments are accounted for in the analysis. Velocities are measured in both cross-shore and alongshore directions with respect to the structure and depth contour (instruments are rotated by −10° with respect to the coordinate system).

On the foreshore, instruments are arranged in a regular grid to capture spatial variations in wave transformation along both cross-shore and alongshore directions, matching the cross-shore positions used in De Ridder et al. (2024), making a direct comparison possible. In addition to these instruments, two arrays: Array 1 (offshore) and Array 2 (nearshore), consisting of wave gauges and velocity instruments, are included to obtain the directional spectrum more reliable than a GRMS or EMS. The offshore array is located on the flat part of the basin, positioned relatively far from the wave maker but also relatively close to GRSM02. During the calibration tests, the nearshore array is located in the center of the basin at the end of the foreshore.

Table 1
This table shows the locations of the measurement instruments. Wave gauge positions represent tests without the structure.

Instrument	x-coordinate [m]	y-coordinate [m]	Combination
WHM01[b]	4.26	30.13	
WHM02[b]	4.75	30.70	
WHM03[b]	4.52	29.42	
WHM04[b]	5.48	30.58	
WHM05[b]	5.31	29.95	
WHM06[b]	5.25	29.30	
WHM07[b]	6.18	29.79	
WHM08	10.91	33.93	
WHM09	7.38	13.93	
WHM10	20.76	32.19	EMS03
WHM11	18.99	22.19	EMS04
WHM12	17.23	12.19	EMS05
WHM13	32.08	30.19	EMS06
WHM14	30.32	20.19	EMS07
WHM15	28.56	10.19	EMS08
WHM16[a]	30.81	20.11	
WHM17[a]	30.98	20.42	EMS09
WHM18[a]	30.85	19.75	
WHM19[a]	31.05	20.07	
WHM20[a]	31.25	20.37	
WHM21[a]	31.14	19.70	
WHM22[a]	31.38	20.01	
WHM23[a]	32.54	19.80	
GRSM01[b]	5.00	30.00	
GRSM02	9.15	23.93	
EMS03	20.72	31.99	WHM10
EMS04	18.96	21.99	WHM11
EMS05	17.20	11.99	WHM12
EMS06	32.05	30.00	WHM13
EMS07	30.28	20.00	WHM14
EMS08	28.52	10.00	WHM15
EMS09[a]	31.01	19.87	WHM17
Q1	28.6	5	
Q2	29.84	10	
Q3	30.28	13	
Q4	30.7	15	
Q5	31.6	20	
Q6	32.48	25	
Q7	33	30	
Q8	34	35	

[a] During tests with the structure, instruments (Array 2) are shifted 5.04 m to the left along the x-axis.
[b] Indicates Array 1.

Waves are generated using 100 piston-type paddles, each 40 cm wide. Second-order wave generation is applied to minimize spurious wave components (Using theory of Van Leeuwen and Klopman, 1996), and the wave board is equipped with active reflection compensation to absorb reflected energy. The effect of second-order steering is shown in Appendix B. The wave conditions are given by a JONSWAP spectrum combined with the directional distribution defined by Eq. (1), with each test lasting for approximately 1000 waves.

Two structures with identical geometry but different crest levels are tested (0.38 m or 0.20 m above the bed level at the toe, see Fig. 2). The crest width is 0.5 m at the water layer thickness measurement section and 0.1 m elsewhere. The structure has a slope $\cot\alpha = 2$, with a double-layer rock armour of $D_{n50} = 23.9$ mm (50 mm thick) and a core of $D_{n50} = 8.5$ mm. The stones are glued together, without affecting the porosity, to prevent movement during the experiments.

Wave overtopping is measured using eight overtopping boxes, each equipped with two wave gauges and one pump. Several overtopping boxes are applied to obtain reliable results for both normal incident and oblique waves which require measurements at different locations. The

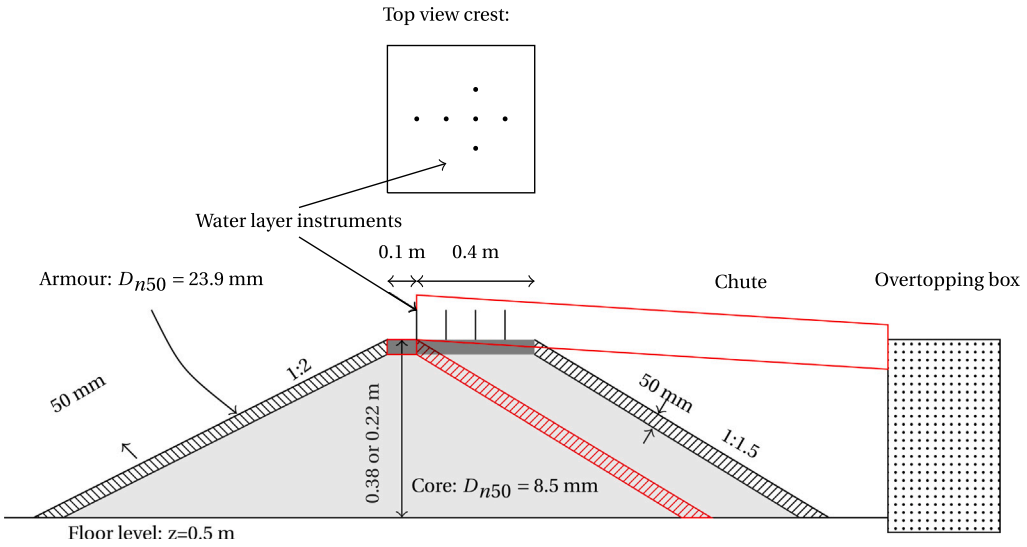

Fig. 2. Cross-section of the rubble mound breakwater(s). The red geometry indicates the cross-sections with the overtopping box, while the black geometry represents the section with the extended crest element used for water layer thickness measurements.

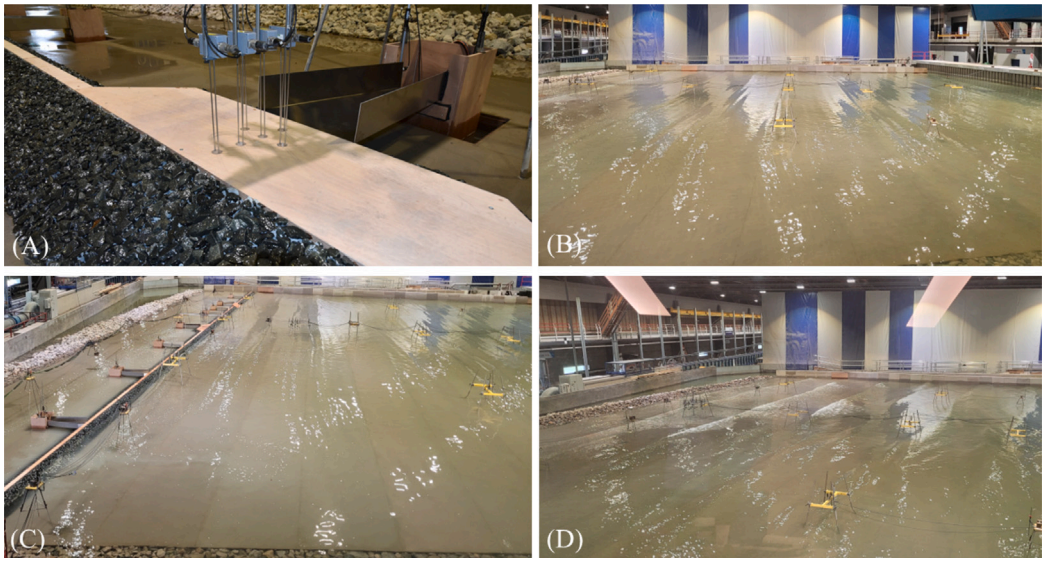

Fig. 3. Photos of the model setup. Panel A shows the crest with the water layer thickness instruments. Panel B shows long-crested wave conditions. Panel C shows the structure and the overtopping boxes. Panel D shows a short-crested wave field.

cumulative overtopping volume is measured by the wave gauges, and when a box is nearly full, water is pumped out. Pumping periods are disregarded in the analysis. The overtopping chute had a width of either 0.5 m or 0.25 m, depending on the test. The water layer thickness is measured with six instruments placed along the crest at an equidistant spacing of 0.1 m: four in the cross-shore direction and two positioned laterally, 0.30 m from the crest and 0.1 m in the lateral direction (see also Fig. 3).

3.2. Test programme

The variations applied in the test programme are summarized in Table 2. Not all possible combinations are tested. For the tests with variations in $\sigma_{\theta,0}$, a full matrix using $s_{m-1,0}$, H_{m0}, h, $\theta_m = 0$, and four values of directional spreading ($\sigma_\theta = 0°, 10°, 20°, 30°$) is applied. The tests with oblique waves are performed with a $\sigma_\theta = 10°$, all variations in $s_{m-1,0}$, and for a subset of H_{m0}. An additional series without directional spreading and with a wave direction of 40° is conducted for a water depth at the wave board of $h_{deep} = 0.63$ m. Tests conditions that would not result in a sufficiently high q are excluded.

Wave directions are defined relative to the structure (or depth contour). Thus, normally incident waves ($\theta_m = 0°$) correspond to $-10°$ relative to the wave maker. Oblique wave conditions with offshore angles of $\theta_m = 40°$ and $\theta_m = 60°$ are generated at angles of 30° and 50°, respectively, relative to the wave maker.

Thus, the following tests are performed:

- Water depths at the wave boards of $h_{deep} = 0.63$ m, $h_{crest} = 0.72$ m and $\theta_{m,0} = 0°$, all variations in H_{m0} (4), $s_{m-1,0}$ (3) and $\sigma_{\theta,0}$ (4) resulting in 48 tests.
- Water depths at the wave boards of $h_{deep} = 0.70$ m, $h_{crest} = 0.63$ m and $\theta_{m,0} = 0°$, all variations in H_{m0} (4), $s_{m-1,0}$ (3) and $\sigma_{\theta,0}$ (4), excluding tests without sufficient overtopping (−6), resulting in 42 tests.
- Oblique waves with $\theta_{m,0} > 0°$ and $\sigma_{\theta,0} = 10°$, the variations in h_{deep} (2), $s_{m-1,0}$ (3) and H_{m0} (3 for $\theta_m = 40°$, 3 for $\theta_m = 60°$ and

Table 2
Variations applied in the physical model experiments (target conditions). Water depth (h_{deep}) and crest height (h_{crest}) are defined with respect to the bottom of the wave flume.

Parameter	Symbol	Variation
Wave height	H_{m0} [m]	0.1, 0.15, 0.2 and 0.25
Deep water wave steepness	$s_{m-1,0}$ [–]	0.015, 0.025 and 0.04
Directional spreading	$\sigma_{\theta,0}$ [°]	0, 10, 20 and 30
Wave direction w.r.t. foreshore	$\theta_{m,0}$ [°]	0, 40 and 60
Foreshore slope	m [–]	1/50
Configurations (Offshore water depth and crest level)	h_{deep} and h_{crest} [m]	I: h_{deep} = 0.70, h_{crest} = 0.88, II: h_{deep} = 0.63, h_{crest} = 0.72

h_{deep} = 0.63 m, and 2 for θ_m = 60° and h = 0.70 m), resulting in 33 tests.

- Oblique waves with $\theta_{m,0}$ = 40°, $\sigma_{\theta,0}$ = 0° and h_{deep} = 0.63 m, the variations in $s_{m-1,0}$ (3) and two wave heights (H_{m0} = 0.15 and 0.20 m), resulting in 6 tests.

Because of the foreshore, the offshore wave parameters differ from those at the structure's toe. The resulting ranges of incident wave conditions at the toe are presented in Table 3, which define the validity limits of the conclusions in this study. The reader is referred to Section 3.3.1 for the definition of the nearshore location.

3.3. Data analysis

An overview of the locations and methods used to compute the various wave parameters is provided in Table 4. For normally incident waves, nearshore wave variables are derived from Array 2, while directional variables come from EMS09. In deep water, Array 1 and GRSM02 are used. For oblique wave conditions, deep-water variables are obtained from GRSM01 and shallow water variables from EMS06. A combination of the Extended Maxium Entrophy Method (EMEM) and the Nonlinear decomposition method for low-frequencies are applied. In the next Sub-sections the selection of the methods and instruments are discussed.

3.3.1. Incident waves

Incident wave conditions are derived from calibration tests without the structure, providing a more reliable estimate, as cross-spectral methods are typically less accurate close to a structure because of a standing wave pattern. An additional benefit is that the resulting formulations reflect conditions unaffected by the structural interference (Similar approach was used in Van Gent, 2021; De Ridder et al., 2024). This aligns with common engineering practice: nearshore wave conditions are first computed using numerical models without the structure, after which empirical formulae are applied to estimate q.

Obtaining nearshore incident wave conditions, including directional information, is challenging, as most methods are not valid for nonlinear breaking waves in shallow water. To address this, several approaches, shown in Table 5, are compared. Four time-domain methods are tested: Linear; Nonlinear; Nonlinear-LF (only for the lower frequencies); and Linear $\eta - u$ (based on free surface elevation and velocity). These time-domain approaches, which are valid for long-crested waves, preserve wave shape (e.g., $H_{2\%}$) and handling phase-locking, while partially accounting for nonlinearity (Eldrup and Lykke Andersen, 2019; De Ridder et al., 2023). However, they cannot be applied to directional sea states. Cross-spectral methods, such as Extended Maximum Entropy Method (EMEM, Hashimoto et al., 1995), Maximum Likelihood Method (MLM, Capon et al., 1967) and Truncated Fourier Series (TFS, Longuet-Higgins, 1963), can estimate a 2D spectrum and thus retrieve incident conditions, but they do not provide wave shape and are not always applicable for standing wave patterns (phase-locking). Recently, Iversen et al. (2025) introduced a time-domain method for directional decomposition under narrow-banded assumptions. It also requires synchronized generation and analysis, as only two directions are possible for each frequency (valid for single-summation generation). While this assumption may hold in deep water, it is less applicable in the nearshore with breaking waves and is therefore not used. In Section 3.3.3 the results of the method provided in Table 5 are discussed.

Table 3
Parameters range of test programme (measured conditions). The incident wave parameters are obtained from wave gauge Set two (toe of the structure).

Parameter	Symbol	Values/Ranges
Seaward structure slope (–)	$\cot\alpha$	2
Armour stone diameter (m)	D_{n50}	0.0239
Water depth at wave board (m)	h_{deep}	0.63 and 0.70
Incident wave height (m)	H_{m0}	0.07–0.13
Incident low-frequency wave height (m)	$H_{m0,LF}$	0.01–0.05
Wave steepness (–)	$s_{m-1,0}$	0.003–0.041
Deep water wave steepness (–)	$s_{m-1,0,deep}$	0.018–0.058
Short-wave steepness (–)	$s_{m-1,0,HF}$	0.012–0.049
Offshore wave directional spreading (°)	$\sigma_{\theta,0}$	7–30
Nearshore wave directional spreading (°)	σ_{θ}	8–25
Offshore mean direction (°)	$\theta_{m,0}$	0–56
Nearshore mean direction (°)	θ_{m}	0–30
Freeboard (m)	R_c	0.09 and 0.18
Foreshore slope (–)	m	0.02
Non-dimensional freeboard (–)	R_c/H_{m0}	0.98–1.94
Non-dimensional stone diameter (–)	D_{n50}/H_{m0}	0.18–0.35
Ratio of low-frequency wave height (–)	$H_{m0,LF}/H_{m0}$	0.15–0.55
Relative water depth normalized by the wave height at toe (–)	h/H_{m0}	1.41–2.15
Relative water depth at toe (–)	kh	0.25–0.68

Table 4
Instrument and applied method to compute the various variables in this study. A distinction is applied between tests with ($\theta_m \neq 0$) and without oblique waves ($\theta_m = 0$).

Variable		Instrument	Method
$H_{m0,deep}$	$\theta_m = 0$	Array 1	Nonlinear-LF
	$\theta_m \neq 0$	GRSM01	Eq. (20)
H_{m0} or $T_{m-1,0}$	$\theta_m = 0$	Array 2	Nonlinear-LF
	$\theta_m \neq 0$	EMS06	Eq. (20)
$H_{m0,LF}$	$\theta_m = 0$	Array 2	Nonlinear-LF
	$\theta_m \neq 0$	EMS06	EMEM
$H_{m0,HF}$ or $T_{m-1,0,HF}$	$\theta_m = 0$	Array 2	HF filter
	$\theta_m \neq 0$	EMS06	HF filter
$\sigma_{\theta,0}$	$\theta_m = 0$	GRSM02	EMEM
	$\theta_m \neq 0$	GRSM01	EMEM
σ_{θ}	$\theta_m = 0$	EMS09	EMEM
	$\theta_m \neq 0$	EMS06	EMEM
$\theta_{m,0}$	$\theta_m = 0$	GRSM02	EMEM
	$\theta_m \neq 0$	GRSM01	EMEM
θ_m	$\theta_m = 0$	EMS09	EMEM
	$\theta_m \neq 0$	EMS06	EMEM
q	$\theta_m = 0$	Q3, Q5 and Q6	–
	$\theta_m \neq 0$	Q1	–
c	$\theta_m = 0$	WHM14, WHM16	–

3.3.2. Wave parameters

Cross-spectral methods do not produce a decomposed signal directly, but instead result in a 2D wave spectrum ($E(f,\theta)$). To decompose the 2D wave spectrum into incident and reflected energy, it is assumed that all the incident energy aligns within $\theta_m - \pi < \theta < \theta_m + \pi$,

Table 5
Overview of applied methods and assumptions to decompose the signals.

Method	Assumptions	Directional information
Linear (Zelt and Skjelbreia, 1993)	Linear long-crested waves	No
Nonlinear (e.g. Eldrup and Lykke Andersen, 2019; De Ridder et al., 2023)	Nonlinear long-crested waves	No
Nonlinear-LF (See approach in De Ridder et al., 2024)	No reflections of short waves and LF wave propagate shore normal	No
Linear $\eta - u$ (Guza et al., 1984)	Linear long-crested waves and shallow water wave celerity	No
EMEM (Hashimoto et al., 1995)	Linear homogeneous wave field	Yes
MLM (derived by Capon et al., 1967)	Linear homogeneous wave field	Yes
TFS (Longuet-Higgins, 1963)	Linear homogeneous wave field	Yes

where θ_m is the mean incident wave direction defined as,

$$\theta_m = \arctan\left(\frac{\sum_j \sum_i \sin(\theta_j) E_{In}(f_i,\theta_j)}{\sum_j \sum_i \cos(\theta_j) E_{In}(f_i,\theta_j)}\right) \tag{11}$$

Thus, $E_{In}(f,\theta)$ is defined as $E_{In}(f,\theta) = E(f, \theta_m - \pi > \theta < \theta_m + \pi)$. The directional spreading is defined as (Kuik et al., 1988),

$$\sigma_\theta = 2\left(1 - \sqrt{\left(\frac{\sum_j \sum_i \sin(\theta_j) E_{In}(f_i,\theta_j)}{\sum\sum E_{In}(f_i,\theta_j)}\right)^2 - \left(\frac{\sum\sum \cos(\theta_j) E_{In}(f_i,\theta_j)}{\sum\sum E_{In}(f_i,\theta_j)}\right)^2}\right) \tag{12}$$

where $E_{In}(f,\theta)$ is the incident energy density, θ is the direction and f is the frequency. To obtain directional variables for specific frequency bands, the index j is restricted. For example, the low-frequency directional parameters are calculated for j ranging in such a way that f ranges between 0 and f_{cutoff}.

From the measured directional wave spectrum, the one-dimensional energy density spectrum is obtained by integrating over the directions,

$$E(f) = \int E(f,\theta) d\theta \tag{13}$$

Given the wave spectrum, the spectral moment is defined as,

$$m_n|_{fmin}^{fmax} = \int_{f_{min}}^{f_{max}} f^n E(f) df \tag{14}$$

where f is the frequency, n the order of the moment, $E(f)$ the 1D energy density, f_{min} the lower frequency and f_{max} the higher frequency. The wave parameters are based on this spectral moment and defined as,

$$H_{m0} = 4\sqrt{m_0} \tag{15}$$

$$H_{m0,LF} = 4\sqrt{m_0|_0^{f_{cutoff}}} \tag{16}$$

$$H_{m0,HF} = 4\sqrt{m_0|_{f_{cutoff}}^{10}} \tag{17}$$

$$T_{m-1,0} = \frac{m_{-1}}{m_0} \tag{18}$$

$$T_{m-1,0,HF} = \frac{m_{-1}|_{f_{cutoff}}^{10}}{m_0|_{f_{cutoff}}^{10}} \tag{19}$$

The cutoff frequency, f_{cutoff}, is defined as $f_p/1.5$, following De Ridder et al. (2024). Expressed in terms of $T_{m-1,0}$ this is $0.60/T_{m-1,0}$.

3.3.3. Verification methods

When analyzing wave variables ($H_{m0,HF}$, $H_{m0,LF}$, and $H_{2\%}$), provided by methods in Table 5 most methods produce similar results in deep water, with only minor deviations for MLM and Linear $\eta - u$ (see Appendix C). In shallow water, however, differences become more pronounced, particularly for $H_{2\%}$ (see Fig. C.21). Therefore, the measured short-wave signal for the test without the structure is assumed to represent the incident short-wave component. For low-frequency waves, the nonlinear decomposition method is applied, as these frequencies contain some reflection even during calibration tests. It is further assumed that directional spreading of low-frequency waves is limited, making the nonlinear decomposition method suitable for normally incident sea states, even with directional spreading. The close agreement between EMEM and the nonlinear decomposition method for $H_{m0,LF}$ supports the validity of this assumption (See Appendix C). The linear $\eta - u$ method would have made it possible to decompose the signal at several locations at the wave basin, but the assumption of a shallow water celerity results in an underestimation compared to the other methods, making the method less reliable.

Directional information must be obtained using a cross-spectral method. Both the offshore wave gauge array and the velocity-free-surface combinations are considered. Although the offshore array generally provides a detailed 2D spectrum, some conditions do not match target values consistently. Therefore, it is chosen to apply the GRSM or EMS (in combination with a wave gauge) to provide the 2D spectrum. This also has the advantage that at several locations in the basin, the directional spectrum is available and obtained with the same method.

In Fig. 4, the deep water results for GRSM02 are shown as a function of the target values for the three cross-spectral methods. Note that the target does not necessarily represent the truth as the wave maker could introduce an error. EMEM shows the closest agreement, especially for $\sigma_{\theta,0}$. The $\sigma_{\theta,0}$ for the MLM and TFS methods varies significantly (Panels D and F) as the directional distribution is, in general, fairly broad for all conditions. Directional spreading of low-frequency waves is also shown to assess the variations of the higher-order waves, even though the method is theoretically invalid for these components. Both the EMEM and MLM show similar results for $\sigma_{\theta,LF}$ and a relationship with the target $\sigma_{\theta,0}$, suggesting that they reasonably capture this part of the spectrum. Since the EMEM shows the best results for σ_θ and the wave parameters (See Appendix C), the EMEM method is applied to obtain the directional wave spectrum.

The accuracy of the EMEM method for obtaining the directional wave spectrum in shallow water cannot be verified as the target value is unknown except for $\theta = 0°$. Also for shallow water, the EMEM method results in the lowest scatter compared to all other methods (comparison not shown for shallow water here). EMEM is therefore considered to be the most suitable method for the conditions in the present test programme.

For oblique wave conditions, the wave gauge array (Array 2) cannot be used to decompose the signal because it does not align with the overtopping box outside the shadow zone. In these cases, $H_{m0,LF}$ is estimated using the EMEM method instead of the nonlinear decomposition method. H_{m0} is then calculated as the energy-based sum (EMEM does not provide a time series) of low-frequency energy from EMEM ($H_{m0,LF,EMEM}$) and the measured high-frequency short-wave energy ($H_{m0,HF}$):

$$H_{m0} = \sqrt{H_{m0,LF,EMEM}^2 + H_{m0,HF}^2} \tag{20}$$

This approach assumes phase independence, which is not fully valid in shallow water. However, the resulting errors are expected to be minimal.

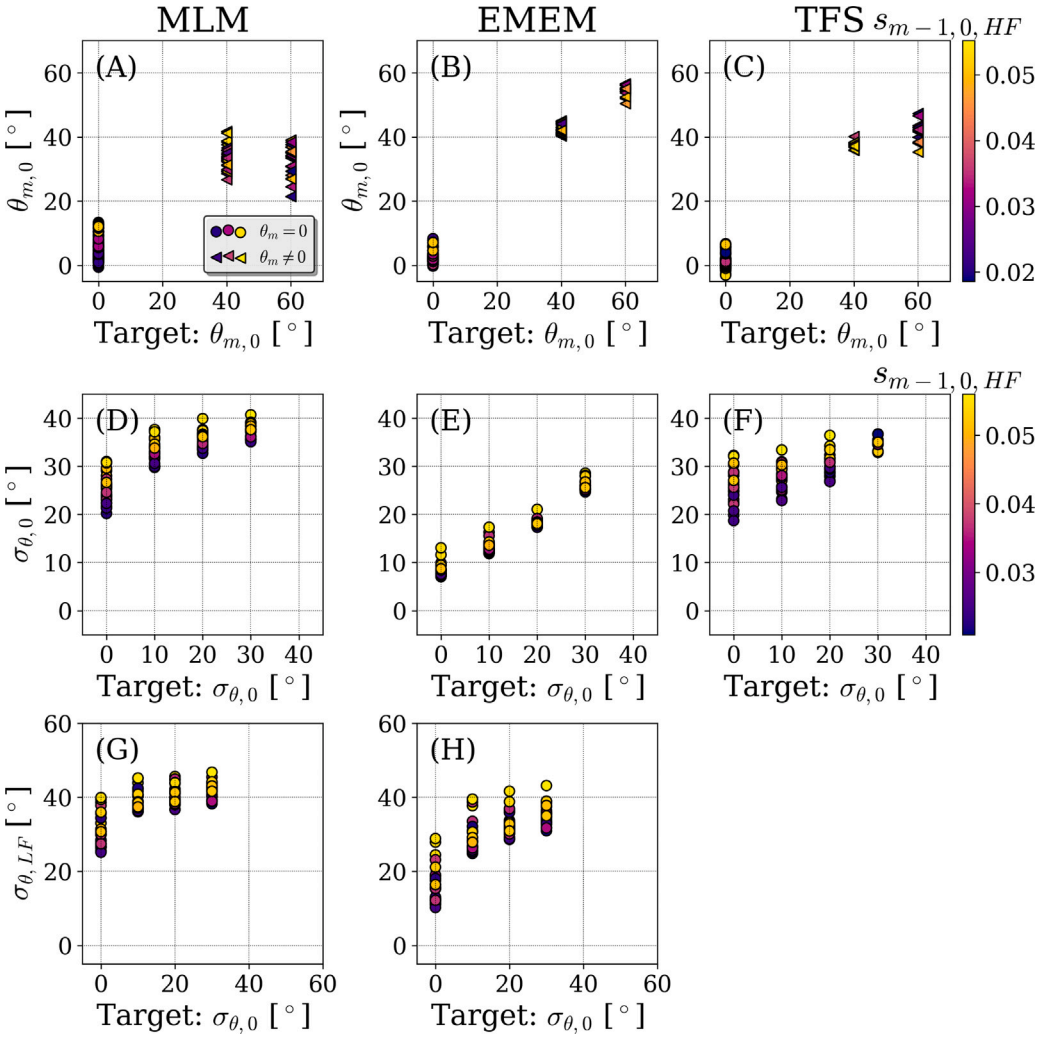

Fig. 4. Comparison of the mean wave direction ($\theta_{m,0}$), directional spreading ($\sigma_{\theta,0}$), and directional spreading of the low-frequencies ($\sigma_{\theta,LF}$) with the target mean direction or directional spreading for the MLM, EMEM, and TFS method. Results are obtained from the offshore instrument GRSM02.

Thus, the EMEM method is used to obtain the directional wave spectrum (characterized by σ_θ and θ_m), while the nonlinear decomposition method is used to obtain incident wave parameters (characterized by: H_{m0} and $T_{m-1,0}$).

3.3.4. Hydrodynamic parameters

In addition to wave parameters, the wave setup, wave celerity, and correlation between low-frequency waves and short wave envelope are computed. Wave setup ($\langle\eta\rangle$) is computed by comparing the mean over the signal before wave generation and during the final segment of the time series (after 5 min). The frequency-dependent wave celerity (c) is estimated from phase differences between two wave gauges (WHM14 and WHM16, as descibed in Thornton and Guza, 1982; Martins et al., 2021). The correlation ($\rho_{\eta_{LF}A}$) between low-frequency waves and the short-wave envelope follows the definition in Janssen et al. (2003).

3.4. Individual events

Next to the mean overtopping discharge, also the individual events are analyzed. These variables are determined using the approach described in De Ridder et al. (2025) using the four water-layer instruments in a row. The water layer thickness (h_i) is based on the maximum water layer signal within an event, which is determined using a peak detection method. Using the consecutive instruments, the front velocity (u_i) is determined for each event by computing the required time shift for the highest correlation between the two signals. The individual volumes (V_i) are obtained by integrating the water layer thickness signal over the event period and multiplying it by the front velocity. The mean value over all instruments is used as the final estimate of the variable Based on h_i, V_i, and u_i, the 2% exceedance values relative to the number of incident waves was calculated ($h_{2\%}$, $V_{2\%}$ and $u_{2\%}$).

3.4.1. Wave overtopping

Several boxes are used to measure q. For normally incident wave conditions, the mean across multiple boxes is taken as an estimate. To determine which boxes are applied to compute the mean, the result from each overtopping box is compared to the results from Box 5 in the center of the structure. This analysis reveals that Boxes 1, 2, and 8 deviate significantly from the others, likely due to their position in the diffraction zone or near the side wall for normal incident waves. Box 4 also shows a deviation, most likely due to its different crest configuration. Therefore, Boxes 3, 5, and 6 produce similar results and are used to calculate q for normal incident waves. In addition to the mean overtopping discharge, the standard deviation across the three boxes is calculated for the normal incident waves. For oblique waves overtopping Box 2 is applied as it is located outside the shadow zone

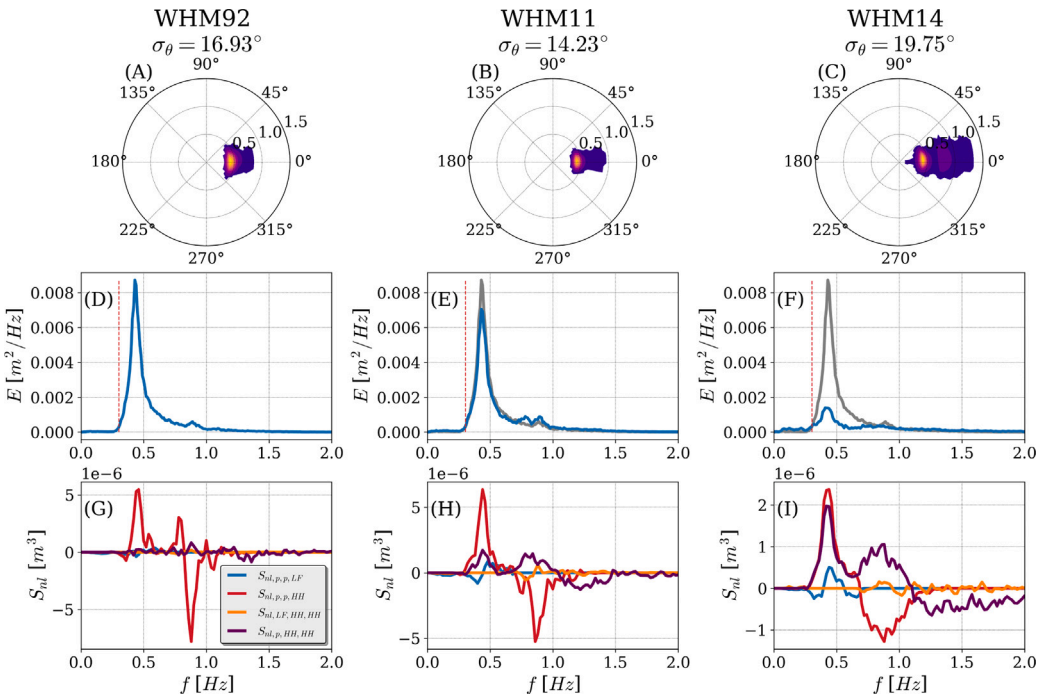

Fig. 5. Directional wave spectrum (Panels A, B, and C), 1D energy density spectrum (Panel D, E, and F), and the dominant nonlinear energy transfers (Panel G, H, and I) for three locations in the basin for Test B721_20. The gray line in the energy density spectrum shows the deep water spectrum and the red dashed line the frequency cutoff. The polar plots in the upper panels show the frequency in Hz on radial axis.

as Overtopping boxes 3 till 8 results in significantly lower volumes for oblique waves.

3.5. Error metrics

The error metric used in this study is the root-mean-square-error (RMSE), root-mean-square-logarithmic-error (RMSLE) or coefficient of determination. The definition of the RMSE and RMSLE are given by Eqs. (21) and (22),

$$RMSE = \sqrt{\left(\frac{1}{N}\sum_{i=1}^{N}(x_i - y_i)^2\right)} \tag{21}$$

$$RMSLE = \sqrt{\left(\frac{1}{N}\sum_{i=1}^{N}(\log(x_i + 1) - \log(y_i + 1))^2\right)} \tag{22}$$

where x_i is the modeled value, y_i the observed value and N the number of values. Next to the RMSE also the coefficient of determination is computed given by,

$$R^2 = 1 - \frac{\sum_{i=1}^{N}(x_i - y_i)^2}{\sum_{i=1}^{N}(y_i - \langle y \rangle)^2} \tag{23}$$

where N is the number of observations, $\langle ... \rangle$ is the mean operator, y_i is the observation and x_i the estimation. The RMS(L)E is a typically applied error measure and the R^2 is a normalized error measure.

4. Wave propagation over the foreshore

To illustrate the wave transformation across the foreshore, Fig. 5 shows the wave spectrum and energy transfer at several locations for Test CB721_20 ($H_{m0} = 0.15$ m, $h = 0.63$ m, $s_{m-1,0} = 0.015$, $\theta_m = 0°$ and $\sigma_{\theta,0} = 20°$). In deep water (Panels A and D), most energy is concentrated near the peak frequency, with relatively broad $\sigma_{\theta,0}$ of about 17° (Panel A). As depth decreases, energy shifts toward both lower and higher frequencies (Panels B and E), forming bound waves aligned with the primary wave in direction.

The nonlinear energy transfer, theoretically only valid for long-crested waves, based on Boussinesq theory (S_{nl}) for various interactions is shown in the lower panels (computed based on Eq. C2 in Henderson et al. (2006) and filtered for three frequency ranges: LF $f < f_p/2$, p $f_p/2 > f > 1.5f_p$ and HH $f > 1.5f_p$). Interactions between two primary waves (indicated with p) primarily transfer energy to higher harmonics (indicated with HH) with the interaction $S_{nl,p,p,HH}$ (Panel H). In very shallow water (Panel I), energy is distributed to even higher harmonics by $S_{nl,p,HH,HH}$ with an interaction of a primary wave first harmonic ($\approx 2f_p$) and second harmonic ($\approx 2f_p$), where it is most likely dissipated. Energy transfer to lower frequencies, mainly given by $S_{nl,p,p,LF}$ is limited in this test. On the other hand, tests with smaller $\sigma_{\theta,0}$ show a larger energy transfer to lower frequencies and therefore more energy at the lower frequencies.

Directional variability decreases due to refraction, narrowing the spreading to approximately 14° (Panel B). In very shallow water, most energy is dissipated, and σ_θ increases again (In Sub-section 4.1.1 this is discussed). Furthermore, the applied cutoff frequency, shown as a dashed red line, nicely separates the low and high frequency wave energy for the three water depths.

4.1. Hydrodynamic variables

The effect of the $\sigma_{\theta,0}$ on the nearshore hydrodynamics is shown in Fig. 6. Two relative water depth variables are shown to plot the results: normalized water depth ($h/H_{m0,deep}$) and the relative water depth (kh) with h the local water depth, $H_{m0,deep}$ the deep water wave height, and k the wave number. The ratio $h/H_{m0,deep}$ primarily reflects the effect of wave breaking, while kh represents the degree of nonlinearity associated with shallow water conditions. Panel A shows the results for both oblique and normal incident conditions, whereas other panels only focus on normal incident conditions.

In Panel A of Fig. 6, the fraction of H_{m0} compared to $H_{m0,deep}$ is shown as a function of $h/H_{m0,deep}$. In agreement with other studies, H_{m0} becomes depth-limited in shallow water (e.g. Battjes and Groenendijk,

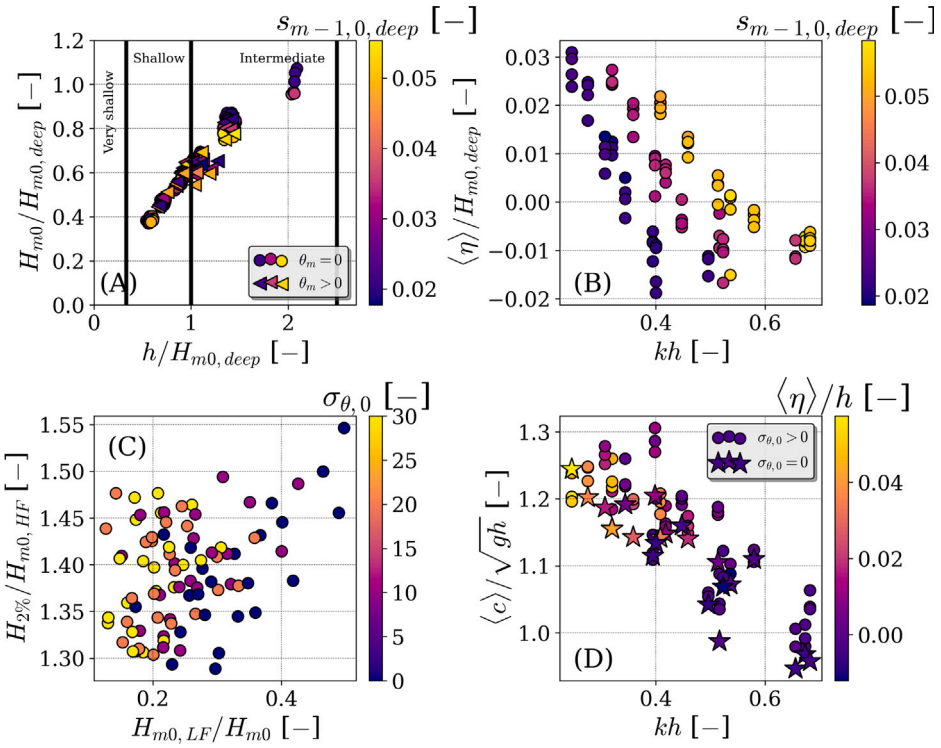

Fig. 6. Normalized wave height as a function of the relative water depth (Panel A), normalized wave setup as a function of the kh, $H_{2\%}/H_{m0}$ as function of $H_{m0,LF}/H_{m0}$ (Panel C), and mean wave celerity as a function of the kh.

2000). Also, H_{m0} has a dependence on the steepness in intermediate water, with a lower H_{m0} for steeper wave conditions, showing steepness-induced dissipation. The directional spreading does not show a notable effect for H_{m0} transformation, at least compared to the energy dissipation by wave breaking. The tests with oblique waves are affected by refraction, which would have a reducing effect on H_{m0} as the water depth decreases in the shoaling zone. However, this effect is not observed for the datasets (Panel A), as wave breaking is the dominant source of the reduction in H_{m0}.

Panel B presents the normalized wave setup ($\langle\eta\rangle$), showing that both the relative depth and the steepness influence the normalized wave setup. Steeper waves produce significantly larger wave setup for a given kh, particularly in deeper water. In very shallow water, the wave setup reaches approximately 2% of $H_{m0,deep}$, which can substantially affect overtopping. No significant effect of the $\sigma_{\theta,0}$ is observed.

The directional spreading $\sigma_{\theta,0}$ does affect $H_{m0,LF}$ (see also Section 4.2), and consequently influences extreme wave heights such as the 2% exceedance height $H_{2\%}$. De Ridder et al. (2024) demonstrated a dependency between $H_{2\%}/H_{m0,HF}$ (1.4 for Rayleigh-distributed waves) and $H_{m0,LF}/H_{m0}$, as conditions with larger $H_{m0,LF}$ lead to higher crest elevations. This trend is also observed here for the long-crested wave conditions (Panel C). For the other conditions, which contain less low-frequency energy, the effect is less pronounced. Thus, conditions with less directional spreading result in a higher value for $H_{2\%}/H_{m0,HF}$ in shallow water.

Panel D presents the mean wave celerity normalized by the theoretical shallow-water celerity, plotted against kh. Wave overtopping is expected to correlate with celerity because higher celerity implies greater momentum and potentially larger overtopping volumes. The results show that for low kh, the wave celerity exceeds the theoretical shallow-water value $\sqrt{gh}$, which may contribute to increased overtopping. Several mechanisms can explain this elevated celerity, including amplitude effects (e.g., Martins et al., 2021), wave setup (shown by the colors of the points), and temporary water-level increases induced by low-frequency waves each of which is linked to kh. Again, no significant influence of $\sigma_{\theta,0}$ is found.

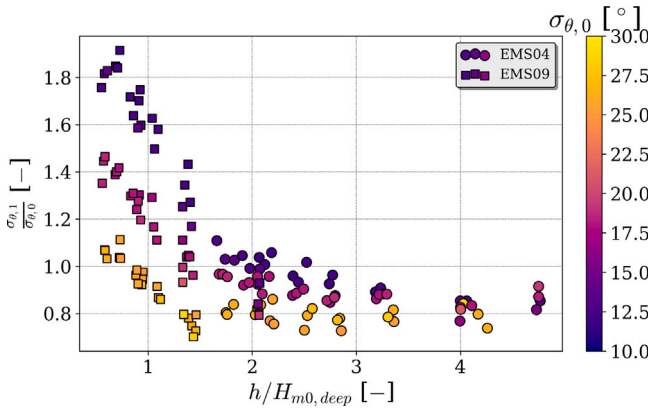

Fig. 7. Ratio of the directional spreading as a function of the deep water directional spreading ($\sigma_{\theta,0}$) at two locations (EMS04 and EMS09). Note that the water depth is defined at the location of the instrument. Only results for $\sigma_{\theta,0}$ larger than zero are shown.

Overall, the hydrodynamic results are coherent and show no outliers. Except for $H_{m0,LF}$ (discussed in the next section), the datasets do not show strong variations in nearshore wave variables as a result of $\sigma_{\theta,0}$, suggesting that q^* is also unlikely to depend strongly on $\sigma_{\theta,0}$ alone.

4.1.1. Refraction of directional spreading

Next to the hydrodynamic variables, also the nearshore directional spreading σ_θ is analyzed. Fig. 7 illustrates its transformation, comparing the deep-water location (GRSM02) with two other positions (EMS04 and EMS09) as a function of $h/H_{m0,deep}$. Due to refraction, σ_θ reduces

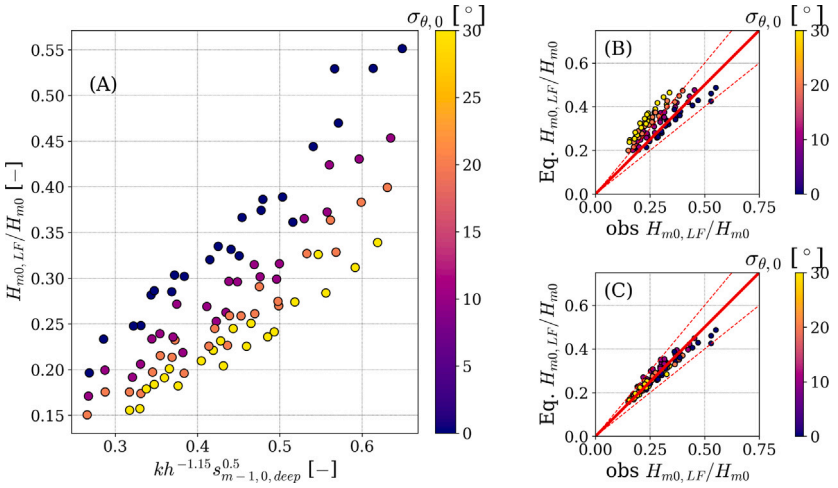

Fig. 8. Relative contribution of low-frequency wave height as a function of $kh^{-1.1.5}s_{m-1,0,deep}^{0.5}$ with the colors indicating the directional spreading in Panel A. Panel B and C show the scatter plot of the non-dimensional wave overtopping discharge computed with Eqs. (24) and (25), respectively. Range of validity: $h/H_{m0} = 1.41 - 2.15$, $\sigma_{\theta,0} = 7° - 30°$, $s_{m-1,0,deep} = 0.018 - 0.058$ and gentle sloping foreshores.

between GRSM02 and EMS04 with approximately 20%. Tests without directional spreading are not shown as the cross-spectral methods are not valid for these conditions and the low spreading values makes the ratio highly sensitive.

In very shallow water (EMS09), σ_θ increases again, especially for the lower directional values. This effect has also been observed and attributed to wave interactions in Herbers et al. (1999), and numerically reproduced by Wei et al. (2017), who explained it as wave amplitude diffraction. It remains uncertain whether this increase is a physical phenomenon or an artifact of the cross-spectral analysis, but the trend appears consistently across all methods considered.

Thus, in shallow water, wave refraction reduces the variability of σ_θ, making it difficult to incorporate the influence of $\sigma_{\theta,0}$ on q^* into an empirical formulation for q based solely on nearshore variables.

4.2. Low-frequency wave height

The amount of low-frequency wave energy strongly depends on directional spreading. Fig. 8 shows the relative contribution of low-frequency energy as a function of $kh^{-1.15}s_{m-1,0,deep}^{0.5}$ (from De Ridder et al. (2024)), with colors indicating the target directional spreading. The figure demonstrates that sea states with little or no directional spreading contain significantly more low-frequency waves. To capture this behavior empirically, both the formulation from De Ridder et al. (2024) and a new formulation are presented in Table 6.

The original expression (Eq. (24)) performs reasonably well, with an RMSE of 0.15 (see Panel C of Fig. 8). However, directional spreading has a substantial effect. To account for this, the term $\frac{s}{100}$ is introduced, with s the directional spreading defined as cosine power (see Eq. (3)) and sea states without directional spreading are specified as $s = 100$. For long-crested conditions, this factor equals one. Including directional spreading in the expression this reduces the RMSE to 0.03 (Panel C, Eq. (25)), a significant improvement compared to RSME of 0.15 without inclusion (Panel B).

5. Overtopping results

5.1. Mean overtopping discharge

The results for the q^* in relation to various parameters are shown in Fig. 9. q^* is plotted against the short-wave steepness ($s_{m-1,0,HF}$), which is found to explain most of the variations in this dataset (see also De Ridder et al., 2024, 2025). The R_c^*, has a lower importance for this dataset because, due to wave breaking, the nearshore wave height does not vary much, especially for the tests where the water depth at the wave board is 0.63 m. Variations caused by the relative crest height are illustrated in Panel A, where most of the scatter arises from the series with a water depth at the wave board of 0.70 m. Panel B shows the effect of directional spreading, which does not reveal a clear trend when showing as a function of $s_{m-1,0,HF}$. However, when compared to the amount of low-frequency wave energy (related to directional spreading), a trend becomes visible (Panel C). For the same wave steepness, tests with more low-frequency energy result in larger q^*. This effect is noticeable only for higher q^*, where low-frequency energy is significant. The reason why the lower q^* do not show significant low-frequency wave energy is shown in Panel D, as the water depth for these data points is in relatively deep water, where the low-frequency wave energy is limited. The six outliers are also obtained from tests in relatively deep water.

Table 6
Expressions for the ratio of the incident low-frequency wave height and the total wave height.

Formulation		$H_{m0,LF}/H_{m0}$ [–]	
		RMSE	R^2
$\frac{H_{m0,LF}}{H_{m0}} = 0.75\ \mathrm{kh}^{-1.15}s_{m-1,0,deep}^{0.50}$	(24)	0.15	0.38
$\frac{H_{m0,LF}}{H_{m0}} = 0.75\ \mathrm{kh}^{-1.15}s_{m-1,0,deep}^{0.50}(s/100)^{0.13}$	(25)	0.03	0.91

The effect of oblique waves is shown in Fig. 10. In this figure, tests with $\theta_m = 0$, which match the wave conditions of one of the oblique wave direction tests are shown. Panel A shows the q^* with respect to the $\theta_{m,0}$ as a function of $s_{m-1,0,HF}$. This panel shows that the q^* reduces as $\theta_{m,0}$ increases, but this is mainly caused by variations in H_{m0}, as demonstrated in Panel B. The tests with $\theta_{m,0}$ not being perpendicular result in a lower H_{m0} and, therefore, in lower R_c^*. When including the $s_{m-1,0,HF}$ next to R_c/H_{m0} on the horizontal axis as shown in Panel C, the spreading decreases but is still present. The effect in terms of θ_m is shown in Panel D, showing that the q^* is lower for the conditions with oblique wave direction. The distinction between the 30° and 50° tests is limited due to the refraction (see Appendix D), as the wave direction at the toe reduces compared to the deep water wave directions.

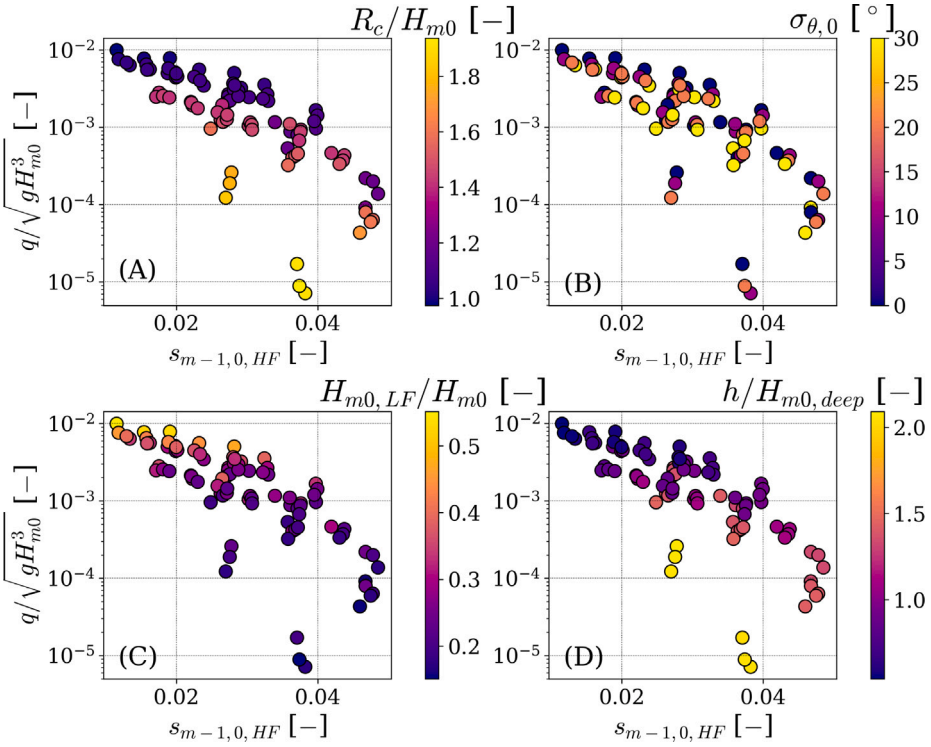

Fig. 9. Non-dimensional mean overtopping discharge ($q/\sqrt{gH_{m0}^3}$) as a function of short wave steepness ($s_{m-1,0,HF}$) where the colors indicate the relative crest height (R_c/H_{m0}, Panel A), directional spreading (σ_θ, Panel B), amount of low-frequency waves ($H_{m0,LF}/H_{m0}$, Panel C) and normalized water depth ($h/H_{m0,deep}$, Panel D).

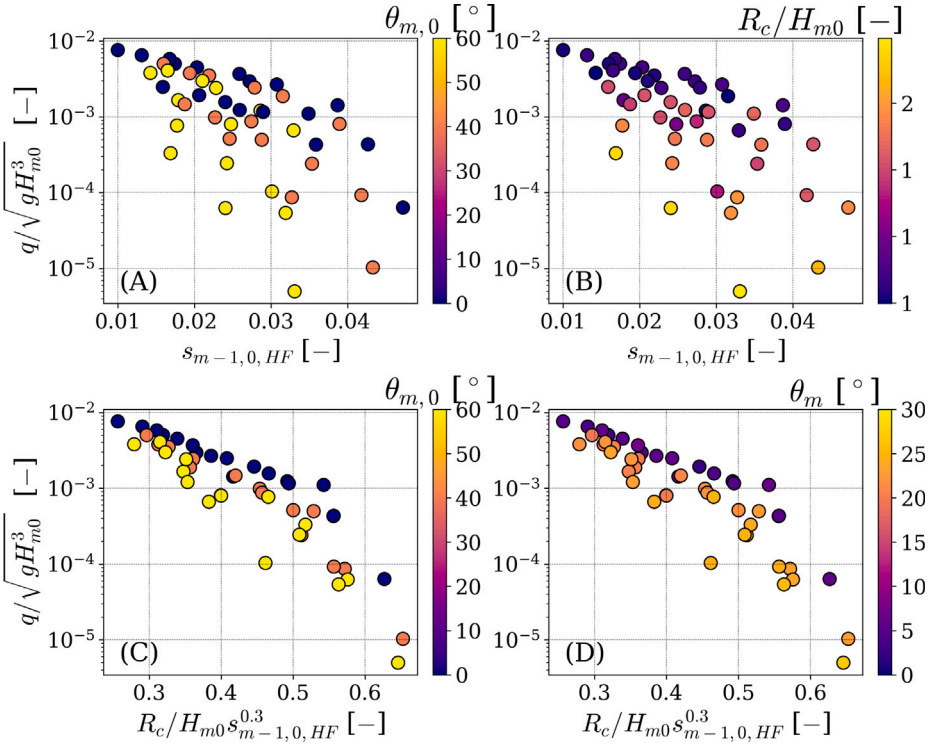

Fig. 10. Non-dimensional wave mean overtopping discharge ($q/\sqrt{gH_{m0}^3}$) as a function of the short-wave steepness ($s_{m-1,0}$, Panel A and B) or relative crest height including the short wave steepness ($s_{m-1,0,HF}$, Panel C and D). Colors indicate offshore mean wave direction ($\theta_{m,0}$, Panel A and C), relative crest height (R_c/H_{m0}, Panel B) or nearshore wave direction (θ_m, Panel D).

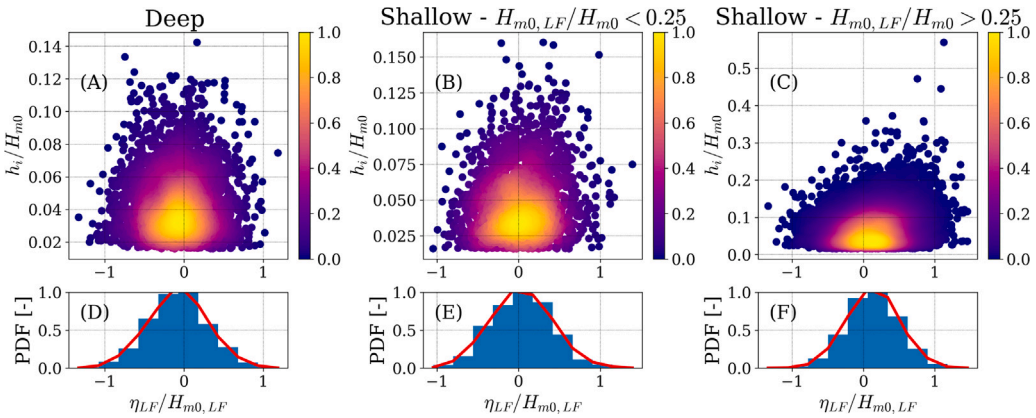

Fig. 11. Non-dimensional water layer thickness as function of the normalized low-frequency wave signal and distribution of the overtopping events as function of the normalized low-frequency wave signal for four different conditions: Deep water low LF (Panel A and D), shallow water low LF (Panel B and E) and shallow water high LF (Panel C and F), Deep is characterized as $h/H_{m0,deep} < 1$.

5.2. Effect of low-frequency waves

The effect of the low-frequency waves on q^* is illustrated by comparing the water layer thickness (h_i), as a proxy for the individual overtopping volumes, at the crest of the structure with the phase of the low-frequency wave (η_{LF}) in Fig. 11. A similar figure was shown in De Ridder et al. (2025), but based on flume experiments (no directional spreading). As $H_{m0,LF}$ is related to the directional spreading, this analysis also contains data points with the same conditions (H_{m0} and $s_{m-1,0,HF}$) but with lower low-frequency waves (the variation in directional spreading). This figure shows three different conditions: deep water (Panel A), shallow water without significant LF waves (Panel B), and shallow water with significant LF waves (Panel C). In this analysis significant LF waves is characterized as $H_{m0,LF}/H_{m0} > 0.25$ and deep water as $h/H_{m0,deep} < 1.0$. This choice is arbitrary but chosen so that the effect is best illustrated.

In deep water (Panels A and D), the low-frequency wave is out of phase with the short waves, meaning that the largest waves travel on top of the trough of the low-frequency wave. This is reflected in the distribution of the overtopping events (Panel D), with most overtopping events at a trough of the low-frequency wave (mean of distribution is at negative η_{LF}). On the other hand, in shallow water, the largest waves can only exist on top of the crest of the low-frequency wave, resulting in the largest overtopping volumes caused by waves traveling at the crest of the low-frequency wave (Panel C) and most overtopping events at positive η_{LF} (Panel F). For the same conditions in shallow water but with less low-frequency energy, this effect is less pronounced (Panels B and E).

Thus, the effect of low-frequency waves is mainly present in shallow water for sea states without significant directional spreading. Furthermore, in shallow water, the low-frequency waves result in larger overtopping volumes (short waves can only exist on top of a LF waves), whereas in deeper water, the volumes will most likely be lower (LF waves result in a water level decrease, not shown). Note that these effects play a role next to the effect depth-induced wave breaking (shown by Victor et al., 2012). In addition, a correction for low-frequency wave energy in the wave overtopping discharge formula is only applicable in shallow water, since the opposite effect is expected in deep water.

5.3. Effect of directional spreading and the offshore conditions

This study intends to derive an expression for q^* based on the nearshore wave conditions. In this way, the expression is independent of the applied foreshore and generally applicable. However, when only q^* based on the nearshore wave conditions is presented, it could give the impression that certain parameters have a minor effect, but when the wave transformation over the foreshore is included, they could have a larger effect. Therefore, in Appendix E, the results are discussed with respect to the wave conditions before the foreshore, emphasizing the combined effect of a foreshore and a coastal structure.

Table 7
Overview of statistical scores for various equations.
* using Eq. (A.3) for the slope ** using Eq. (A.3) for the slope and Eq. (10) for the effect of the directional spreading.

Formulation	$q/\sqrt{gH_{m0}^3}$ [−]	
	RMSLE	R^2
Eq. (7) (Van Gent, 1999)	1.33	<0
Eq. (6) (TAW, 2002)	1.35	<0
Eq. (7)* (Altomare et al., 2016)	1.24	<0
Eq. (8) (EurOtop, 2018)	3.43	<0
Eq. (7)** (Altomare et al., 2020)	1.40	<0
Eq. (A.1) (De Ridder et al., 2024)	0.63	0.85
Eq. (A.2) (De Ridder et al., 2024)	0.65	0.84
Van Gent et al. (2025)	0.83	0.39

The $s_{m-1,0,deep}$ and $R_c/H_{m0,deep}$ are the most important factors influencing q^*, both affecting q^* in order of several factors of 10 (determined visually using Fig. E.23). For low $R_c/H_{m0,deep}$, the $s_{m-1,0,deep}$ shows a lower effect compared to higher $R_c/H_{m0,deep}$. The effect of the directional spreading is an order of magnitude smaller, but still relevant. The last variation applied is the water depth, which is negligible for these conditions.

To show the effect of directional spreading, the relative difference with the results without directional spreading ($\sigma_\theta = 0°$) is shown in Fig. 12. Both the q and q^* show a reduction when the directional spreading increases. The average of all datapoints is approximately 80% for the 10° of directional spreading and further reduces to approximately 60% for 30° relative to no direction spreading. The same is also observed for q^*, showing that this reduction is not caused by variations in H_{m0}. H_{m0} is slightly lower when the directional spreading increases, but this is limited (average change of about 4%). On the other hand, $H_{m0,LF}$ is significantly reduced. Thus, the offshore directional spreading itself does not necessarily result in a reduction of q^*, whereas it does affect the low-frequency wave and thereby q^*. Same findings are found for the individual overtopping events ($h_{2\%}$ and $V_{2\%}$), see Appendix H.

5.4. Consistency with previous work

The long-crested wave conditions in this test campaign are similar to tests performed in De Ridder et al. (2025), where the same test conditions were performed in the flume (Series A7 and A3 in De Ridder

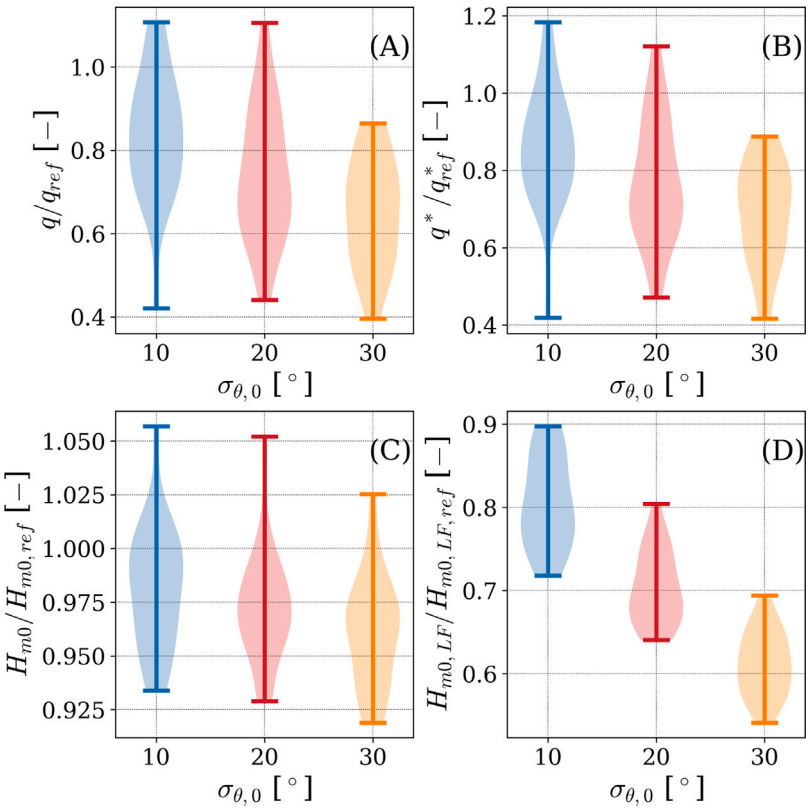

Fig. 12. Violin plot for the relative mean overtopping discharge (Panel A), non-dimensional mean overtopping discharge (Panel B), wave height (Panel C), and low-frequency wave height (Panel D) compared to the results for 0 degree of directional spreading.

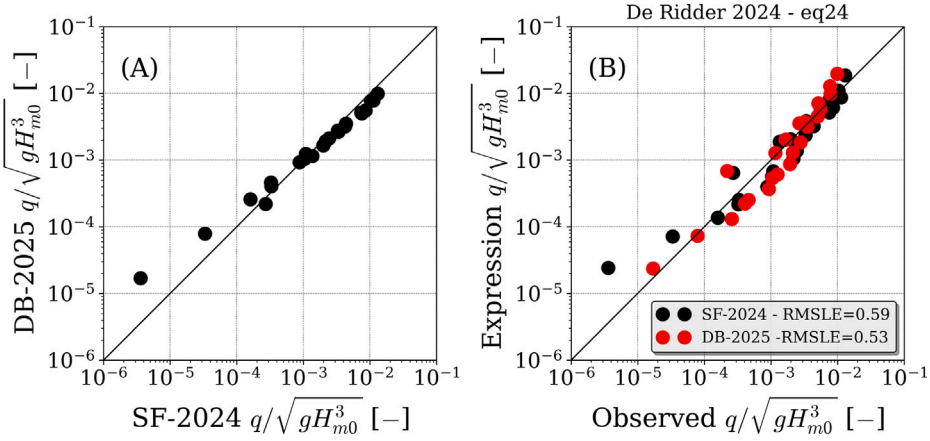

Fig. 13. Comparison of the SF-2024 and DB-2025 results for the non-dimensional wave overtopping discharge (Panel A). Panel B shows the results for the expression presented in De Ridder et al. (2024), Eq. (A.1) for non-dimensional wave overtopping discharge.

et al. (2025)). To verify the consistency between the current dataset (Delta Basin, DB-2025) with the previous dataset (Scheldt Flume, SF-2024), the results for q^* is shown in Fig. 13 for normal incident long crested wave conditions.

These results show that q^* are very similar, but that there is a small bias between the two experiments. This difference is not caused by variations in H_{m0}, as no bias is found when comparing H_{m0} (not shown). Therefore, these deviations are considered to result from the model setup. In Panel B, the expression found in De Ridder et al. (2024), Eq. (A.1) is verified for both subsets, showing that this expression performs reasonably well for this dataset. The RMSLE is even lower for this new dataset, with an RMSLE of 0.53. Thus, it can be concluded that both datasets are consistent and that the existing formulation also holds for the new experiments without directional spreading.

5.5. Comparison with existing formulations

Several formulations from the literature for predicting q^* are evaluated using this dataset, see Table 7 and Fig. 14.

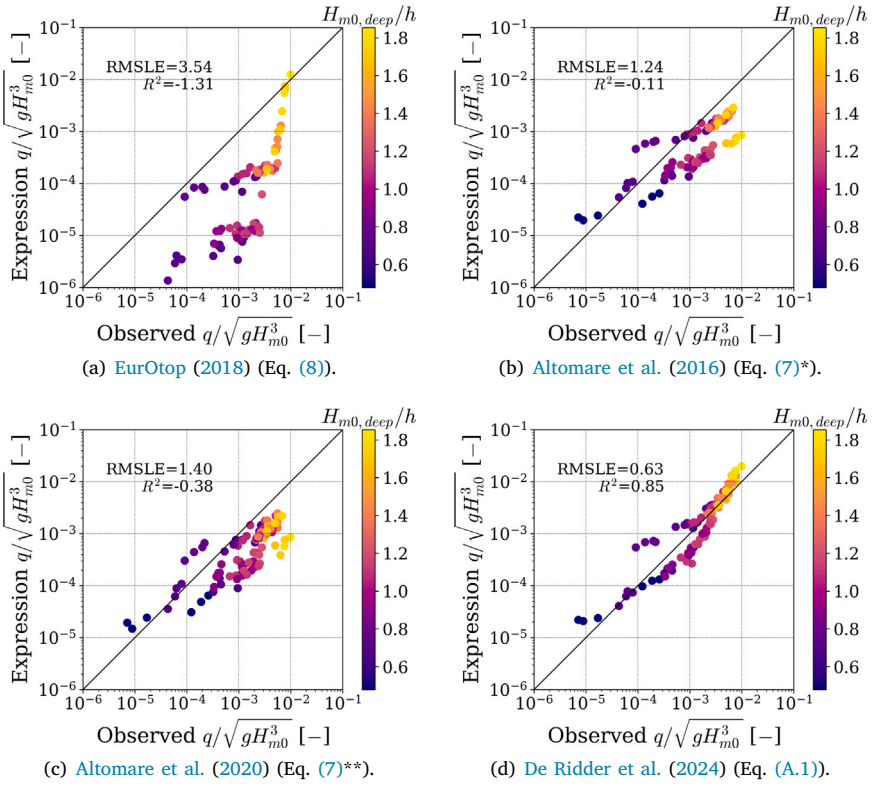

(a) EurOtop (2018) (Eq. (8)). (b) Altomare et al. (2016) (Eq. (7)*).

(c) Altomare et al. (2020) (Eq. (7)**). (d) De Ridder et al. (2024) (Eq. (A.1)).

Fig. 14. Scatter plots of several existing formulations.

The EurOtop (2018) formulation performs worst, as it does not account for the wave steepness, resulting in larger scatter (see Panel A of Fig. 14). TAW (2002) formulation shows improved accuracy (RMSLE = 1.35). Eq. (7) for shallow water of Van Gent (1999) performs better, and the modified version of Eq. (7) by Altomare et al. (2016) slightly reduces the error even further (see Panel B of Fig. 14). However, incorporating directional spreading in Eq. (7) as proposed by Altomare et al. (2020) decreases the accuracy (see also Panel C of Fig. 14). This can be explained by the fact that directional spreading itself is not the direct driver of wave overtopping, but the amount of low-frequency energy affected by directional spreading (see also Appendix F). An influence factor based solely on directional spreading cannot consistently result in accurate predictions, because the magnitude of low-frequency waves also depends on the local water depth. The formulation by Van Gent et al. (2025), also performs well (RMSLE = 0.83), with the advantage that the short-wave steepness is not required.

The best results are obtained with the formulations from De Ridder et al. (2024), see Eqs. (A.1) and (A.2), which was developed using similar experiments (see also Panel D of Fig. 14). The high accuracy of Eq. (A.1) (RMSLE = 0.63) demonstrates that combining $s_{m-1,0,HF}$ with R_c^* provides reliable estimates. However, including $H_{m0,LF}$ does not improve the accuracy (Eq. (A.2)), indicating that for conditions with directional spreading the effects of low-frequency energy are not sufficiently captured. Thus, in the next section, these formulations are adjusted to correctly incorporate the effect of $H_{m0,LF}$ for conditions with and without directional spreading.

6. Fit of a new empirical formulation

Previous results indicate the need for an expression that accounts for directional spreading through $H_{m0,LF}$. This section derives such an expression. First, key parameters and their correlations are analyzed. Next, assuming variable independence, the influence of individual wave parameters is demonstrated by introducing them sequentially. Third, the existing expression for the oblique wave attack influence factor is verified for shallow water. Finally, several expressions with increasing complexity are derived using a nonlinear optimization method.

6.1. Selection of explanatory variables

Here, correlations between the potential explanatory variables are verified (see Fig. 15). While complete independence between variables cannot always be achieved, it is generally preferred, as this allows the physical process to be represented by a single (non-)dimensional parameter. Moreover, independent parameters prevent a behavior from being captured indirectly by "wrong" parameters, making it harder to include other processes in the expression later on. The wave variables selected in this section are known to be relevant in shallow water, as demonstrated in the variable assessment by De Ridder et al. (2024).

First, the normalization of the relative crest height is discussed. The crest height can be normalized with H_{m0} or $H_{m0,HF}$. The first would contain a normalization with all wave energy, whereas the latter mainly contains the short-waves that actually overtop the structure. In the upper panels (Panels A, B, and C), both ways of normalization are shown as a function of $s_{m-1,0,HF}$ or $s_{m-1,0}$. These panels show that for approximately the same relative crest height, the data points have a more or less straight line when using the $H_{m0,HF}$ in the relative crest height (Panel A), especially for the lower relative crest height ($R_c/H_{m0} \approx 1$). When using H_{m0}, the data points increase for an increasing $s_{m-1,0}$ (Panel B), because $H_{m0,LF}$ increases for a decreasing $s_{m-1,0,HF}$. The same is observed when H_{m0} and $s_{m-1,0}$ is applied (Panel C). When the effect of $H_{m0,LF}$ is accounted for in the expression, it

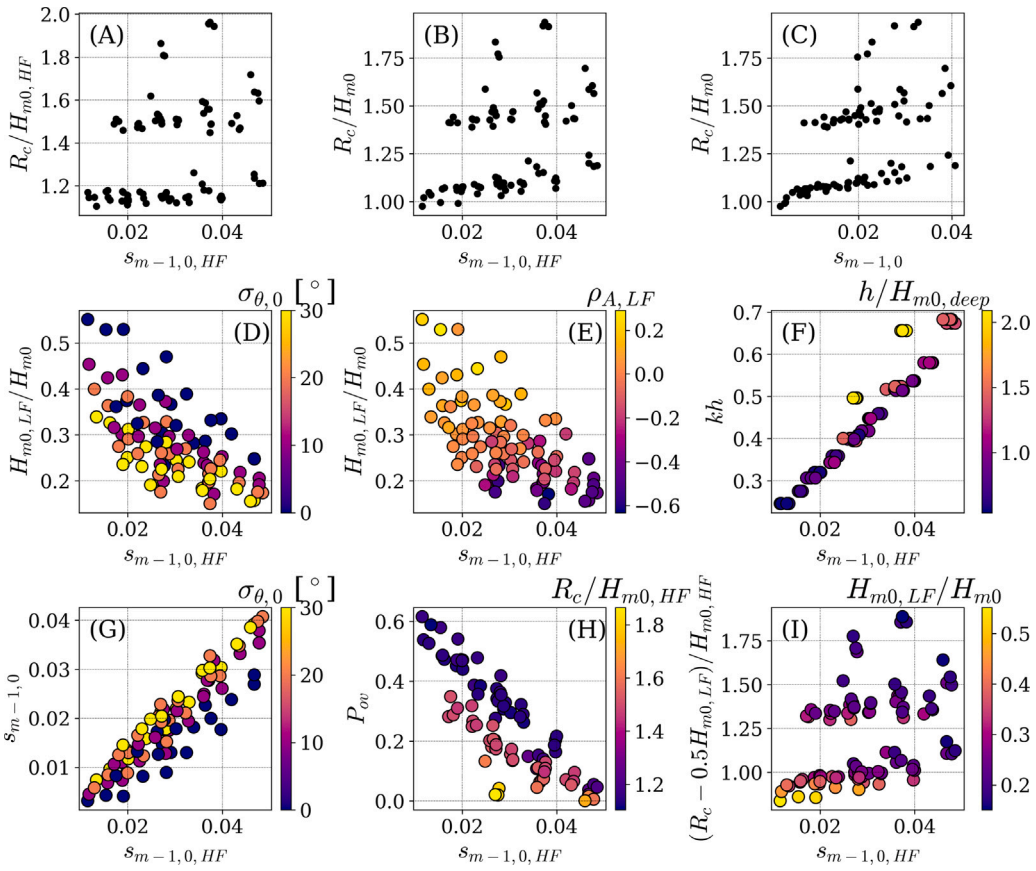

Fig. 15. Correlations between several wave parameters. Panels A, B, and C show the (short-) wave steepness as a function of the relative crest height. Panels D and E show the short-wave steepness as a function of the ratio of low-frequency wave height, where the colors represent the directional spreading. Panel D and E show the correlation between short-waves and low-frequency waves, where the color represents the directional spreading (Panel D) and the correlation between the short and long waves. Panel F shows the short-wave steepness as a function of the relative depth, where the colors represent the normalized water depth. Panel G shows the short-wave steepness as a function of the number of overtopping events, with the relative crest height as color. Panel H shows the short-wave steepness as a function of the wave steepness with the directional spreading as colors. Panel I shows the adjusted relative crest height as a function of the short-wave steepness, with the low-frequency ratio as color.

is preferred that it does not affect the relative crest height itself, and therefore, $H_{m0,HF}$ is preferred.

Second, the correlation between the ratio of $H_{m0,LF}$ and $s_{m-1,0,HF}$ is lower than found for long-crested wave conditions (De Ridder et al., 2024, Panel D). The variation in $\sigma_{\theta,0}$ results in more variation for the same $s_{m-1,0,HF}$. This increased spreading makes it easier to distinguish between the effects of $H_{m0,LF}$ and $s_{m-1,0,HF}$ with the current dataset.

Third, it is verified whether the low-frequency waves result in an increase of q^* by plotting the correlation ($\rho_{\eta_{LF}A}$, Pearsons's correlation (Pearson, 1895)) between the low-frequency waves (η_{LF}) and the short waves envelope (A, Panel E). In deeper water, where this correlation is negative, meaning that the largest short waves are on top of the trough of the low-frequency wave (reducing the maximum crest height), whereas this correlation is positive in the surfzone, with short waves on top of the crest of the low-frequency wave. Panel E shows that for all conditions with a significant amount of low-frequency energy, this correlation is positive, meaning that for all these conditions, the short waves travel on top of the crest of the low-frequency wave. Therefore, low-frequency waves likely increase q^* (see also Section 5.2).

Fourth, $H_{m0,LF}$ (see Fig. 8) and other hydrodynamic variables (see Fig. 6) are dependent on kh. In Panel F, it is shown that for shallow water, kh and $s_{m-1,0,HF}$ are highly correlated, making $s_{m-1,0,HF}$ also a relevant variable to include in the expression when considering shallow water. In addition, the effect of different definitions of the wave steepness is shown in Panel G. The distinction between short and long waves is not relevant for sea states with significant directional spreading, as the low-frequency growth is limited. However, for sea states without significant directional spreading, differences in the wave steepness are observed, making the $s_{m-1,0,HF}$ the preferred variable.

Fifth, the effect of the relative crest height and $s_{m-1,0,HF}$ on the number of overtopping events is shown in Panel H, showing that both variables affect the P_{ov}. For low $s_{m-1,0,HF}$ conditions with a low relative crest height, up to 60% of the waves cause overtopping, whereas higher crest heights result in significantly fewer overtopping events. As q is largely dependent on P_{ov}, this illustrates that both R_c/H_{m0} and $s_{m-1,0,HF}$ are the most important variables for q.

Thus, a relative crest height defined in terms of $H_{m0,HF}$, with a $s_{m-1,0,HF}$ and $H_{m0,LF}$, is the preferred set of variables. The dependency of these variables are illustrated in Panel I with the relative crest height adjusted with $H_{m0,HF}$. Thus, for conditions with significant low-frequency wave energy, the relative crest is reduced.

6.2. Step-by-step approach

To illustrate the development of the proposed expression for q^*, variables are introduced sequentially (Fig. 16), under the assumption that all variables are independent. Results are shown for both the

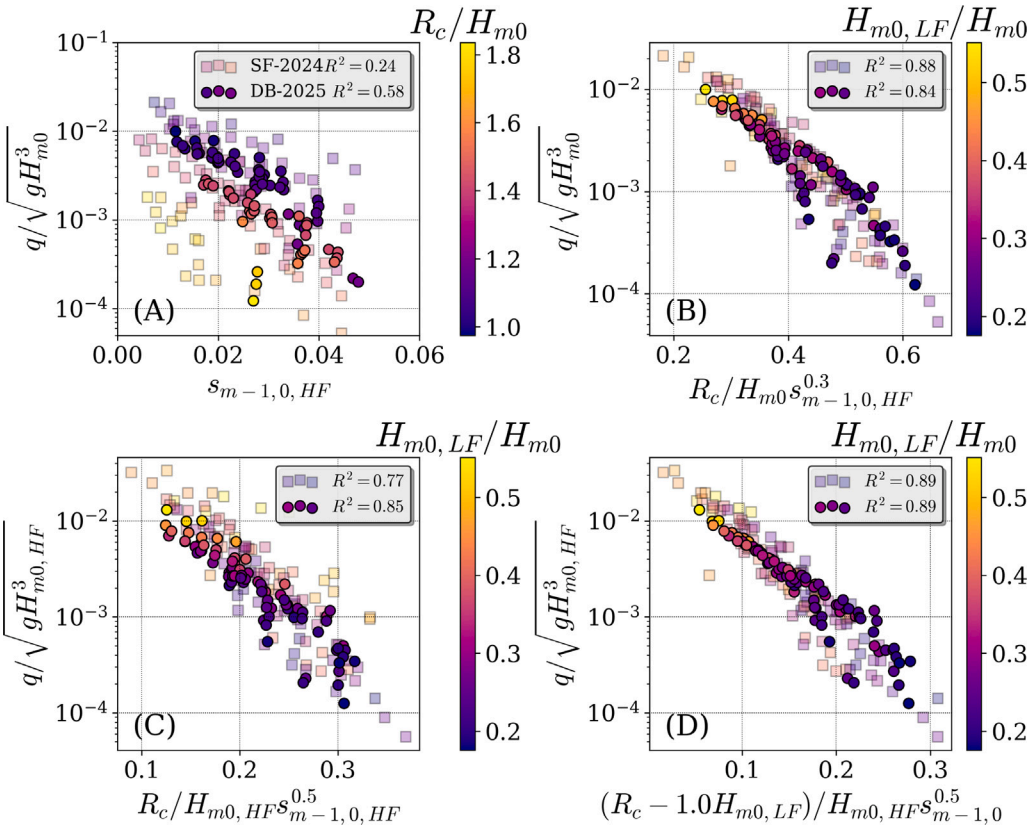

Fig. 16. q^* as a function of $s_{m-1,0,HF}$ (panel A), $R_c/H_{m0}s_{m-1,0}^{0.3}$ (Panel B), $R_c/H_{m0,HF}s_{m-1,0}^{0.5}$ (Panel C), and $(R_c - H_{m0,LF})/H_{m0,HF}s_{m-1,0}^{0.5}$ (Panel D) for both DB-2025 and SF-2024.

present dataset (DB-2025) and the dataset described by De Ridder et al. (2024, SF-2024). The same analysis is performed for the $h_{2\%}$ in Appendix H.

The first step combines $s_{m-1,0,HF}$ with R_c/H_{m0}, which leads to a substantial improvement in the fit (Panels A and B). A power of 0.3 for $s_{m-1,0,HF}$ is required to reduce scatter, resulting in an R^2 of 0.84 for DB-2025.

However, as argued in Section 6.1, normalization with $H_{m0,HF}$ is preferred. This adjustment is implemented in Panel C, where H_{m0} is replaced by $H_{m0,HF}$. Consequently, the exponent of $s_{m-1,0,HF}$ is increased to 0.5. Although this step does not improve overall accuracy, it clarifies the influence of $H_{m0,LF}$ (Panel C). Moreover, this modification is essential for combining the two datasets. While adjusting coefficients can improve the fit for one dataset when using H_{m0}, it does not yield satisfactory results for both datasets simultaneously.

In Panel D, the effect of $H_{m0,LF}$ is incorporated into the relative crest height, resulting in an R^2 of 0.89 for DB-2025. Data points with high values of $q/\sqrt{gH_{m0,HF}^3}$ predominantly occur in shallow water, where low-frequency energy effects are most pronounced. In contrast, smaller q^* are generally associated with deeper water depths, leading to lower values of $H_{m0,LF}$. The remaining scatter at low q^* is likely attributable to measurement uncertainty, which is relatively large for small q^*.

6.3. Effect oblique waves

The effect of oblique waves is quantified using an influence factor (γ_β), obtained by comparing the q^* for normally incident waves ($q^*_{\theta_m=0}$) with the oblique wave tests ($q^*_{\theta_m>0}$) for the same set of conditions. A direct comparison is not possible as nearshore wave conditions differ between the tests. Therefore, an exponential fit, Relating q^* to the relative crest height (R_c^*) defined as

$$R_c^* = \frac{R_c}{H_{m0}s_{m-1,0,HF}^{0.3}},$$

was applied to tests without oblique waves and compared to the corresponding test with oblique wave attack ($\sigma_\theta = 10°$ and $H_{m0} > 0.10$ m). $H_{m0,LF}$ is not included in this analysis, as the number of data points is limited and only one value of the directional spreading is used. Using this relationship between q^* and R_c^*, the expected q^* for oblique wave tests was computed based on the nearshore conditions. This analysis was performed for overtopping Box 1 (EMS03), Box 4 (EMS09) and Box 6 (EMS08), providing variation in wave directions as Boxes 4 and 6 are located in the shadow zone (thus also have lower H_{m0}). The ratio $\ln q^*_{\theta_m=0}/\ln q^*_{\theta_m>0}$ yields an estimate of the influence factor (γ_β), shown in Fig. 17 as a function of nearshore wave direction. This approach is only applicable to an overtopping formulation where no additional variables are in front of the exponent or when powers are applied to the relative crest, which is the case for the expressions in this manuscript (See also the appendix of Van Gent, 2022).

Although this method provides only a rough estimate, the results reveal a clear trend: the influence factor decreases with increasing wave obliquity. For all points with a wave direction larger than 20°, the reduction factor is smaller than 1. The results from Boxes 4 and 6 (EMS09 and EMS08) show that for a smaller wave direction, the effect is minimal with γ_β close to one. Also, the scatter for these boxes is larger as q^* is lower for these boxes, making the measurement error relatively larger.

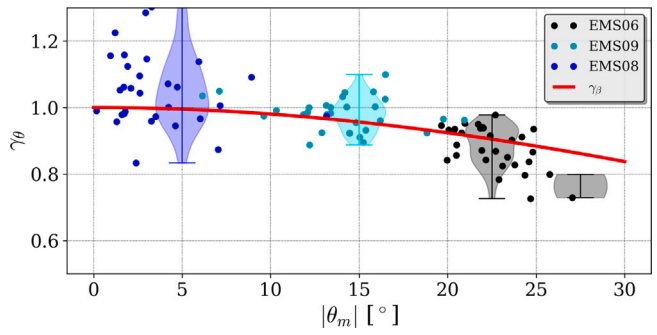

Fig. 17. Influence factor for the wave direction (γ_β) as function of the nearshore wave directions. Results are obtained from the tests with oblique wave attack at overtopping box 1 (EMS06), 4 (EMS09), and 6 (EMS08). Violin plots are shown for wave direction between: 0–10, 10–20, 20–25, and 25–3°. The influence factor of van Gent and van der Werf (2019) is shown by a red curve.

The formulation of ($\gamma_\beta = 0.65\cos^2(|\theta|) + 0.35$, van Gent and van der Werf, 2019) is capturing the trend reasonably well, suggesting that the same influence factor is also valid for shallow water.

6.4. Expression for the mean overtopping discharge

Several expressions are fitted using a nonlinear optimization method (Levenberg–Marquardt algorithm Levenberg, 1944; Marquardt, 1963) that minimizes the sum of the squares of the differences between the observation and the prediction. To take the measurement uncertainty into account, the standard deviation of q (see Section 3.4.1) is included as a weight for the DB-2025 tests. For the SF-2024 tests, an estimate of the std. given by $q^*/10$ is applied. A bootstrapping technique is applied to obtain a robust estimate of the coefficient. Every fit is performed 150 times with a dataset of N elements from the total dataset, with N elements meaning that entries can be present multiple times or not at all. The mean coefficient is applied as a final estimate, and the 95% percentile of the coefficients is shown in Appendix G for two relevant expressions, showing the influence of the coefficient. Moreover, the roughness factor is set to a constant value of 0.55.

The final expressions are evaluated for four different subsets: the experiment described in this manuscript with normal incident waves (DB-2025, $\theta_m = 0$), the experiment described in this manuscript with oblique incident waves (DB-2025, $\theta_m > 0$), the experiments in De Ridder et al. (2024) (SF-2024), and the combined dateset. The final fit is based on subsets DB-2025 (with $\theta_m = 0$) and SF-2024 with only q^* larger than 10^{-5}. The DB-2025 dataset better captures the influence of $H_{m0,LF}$, as it is an independent variable, whereas DF-2024 includes more variations in R_c/H_{m0}.

In Table 8, the accuracy of several expressions fitted on the entire dataset are shown for the various subsets. These results highlight a few important findings. First, only considering the relative crest height gives a poor estimate with an $R^2 = 0.47$ (RMSLE of 0.87) for all the data points. Including $s_{m-1,0}$ significantly improves the accuracy with an $R^2 = 0.75$ (RMSLE of 0.60). As shown in De Ridder et al. (2024), $s_{m-1,0,HF}$ results in even a higher accuracy ($R^2 = 0.83$ and RMSLE = 0.50). When the fit would have been performed on purely the DB-2025 data, the effect of the type of wave steepness is less pronounced (not shown), but when the flume experiments are included with significant energy at the low-frequency part, the short-wave steepness is preferred.

In Eq. (29), the effect of oblique waves is demonstrated by neglecting the influence factor for oblique waves leading to a significantly higher error for the $\theta_m > 0$ tests. The R^2 increases from 0.22 (RMSLE = 0.94) to 0.73 (RMSLE = 0.55) when γ_β is included.

To account for $H_{m0,LF}$, three formulations are proposed where $R_c/H_{m0,HF}$ is adjusted with $H_{m0,LF}$. An expression using $s_{m-1,0}$, an expression using $s_{m-1,0,HF}$, and an expression using $s_{m-1,0,HF}$ in combination with $H_{m0,HF}$ as normalization are applied. In contrast to De Ridder et al. (2024), the roughness factor is included as a factor in front $R_c - H_{m0,LF}/H_{m0}$ to make the roughness factor independent of the relative crest definition.

When using $s_{m-1,0}$ and $H_{m0,LF}$ as shown in Eq. (30), the accuracy does not improve compared to Eq. (28), most likely because the low-frequency contribution is accounted for twice, both in $s_{m-1,0}$ and $H_{m0,LF}$. The expression including $s_{m-1,0,HF}$ (Eq. (31)) shows an improvement with Eq. (28). For the combined dataset the effect is minimal with a $R^2 = 0.84$, but for the DB-2025 ($\theta_m = 0$) dataset the improvement is more significant ($R^2 = 0.85$). A second small improvement is found when using $H_{m0,HF}$ as normalization (Eq. (32)). As shown in Fig. 15, this normalization results in more independent variables, making the formulation more robust.

Thus Eq. (32) is the preferred equation when accounting for $H_{m0,LF}$ and thereby accounting for $\sigma_{\theta,0}$. However, Eq. (28) is also relatively accurate (see also Fig. 18) and can be applied when $H_{m0,LF}$ is not available. These formulations are available at the Coastal Structures Toolbox: https://deltares-coastal-structures-toolbox.readthedocs.io/en/stable/.

The proposed formulations are valid for shallow water ($h/H_{m0} = 1.41 - 2.15$ for DB-2025) with sea states with $s_{m-1,0,HF} = 0.012$–0.049, $\theta_m = 0$–$030°$ and $\sigma_\theta = 8$–$25°$. Moreover, the findings are valid for gentle sloping profiles and relative crest height between 0.98 and 1.94. It should not be applied in deep water or extremely shallow water where only the low-frequency waves cause the wave overtopping.

7. Discussion

One of the difficulties of fitting an empirical formulation is the dependence between variables. While variations in hydrodynamic parameters (e.g., $H_{m0,LF}$) span the full parameter space, covering kh, $\sigma_{\theta,0}$, and $s_{m-1,0,HF}$, and therefore make those findings broadly applicable, the parameters relevant to q^* do not cover the entire parameter space. Furthermore several parameters are correlated, complicating efforts to isolate individual effects. In the De Ridder et al. (2024) dataset, for example, low-frequency wave effects were difficult to separate because they were strongly correlated with $s_{m-1,0,HF}$. In contrast, the new dataset provides a more reliable basis for fitting a formulation, as this correlation is reduced due to variations in σ_θ. Furthermore, most data points share a similar relative crest height because H_{m0} remains relatively constant under depth-limited conditions, making the variation in R_c/H_{m0} limited. Therefore, it is recommended to verify the formulation also for more variations in relative crest height. This would also help to confirm the role of low-frequency waves for smaller overtopping volumes, as their influence in the current dataset is most pronounced for larger volumes.

The results also show that several processes affect the wave overtopping in shallow water, making it harder to account for all these processes in one empirical expression. Therefore, it is hypothesized that the accuracy of a simple empirical expression for shallow water has an upper limit. Next to empirical formulations, other methods are available to obtain the q for more complex cases, using, for example, machine learning techniques (e.g. Mares-Nasarre et al., 2021; Den Bieman et al., 2021), numerical models (e.g. Chen et al., 2022; Irías Mata and Van Gent, 2023) and probabilistic models (Mares-Nasarre, 2025). It is therefore also recommended to verify or expand these methods for shallow water conditions.

The effect of wave direction on wave overtopping is shown (Fig. 17), but the amount of scatter in the present data set with shallow foreshores is significant. Several reasons are identified that cause this scatter. First, in contrast to deep water, it is difficult to obtain the same nearshore

Table 8
Overview of RMSLE and R^2 for various equations and datasets.

Formulation		$q/\sqrt{gH_{m0}^3}$ or $q/\sqrt{gH_{m0,HF}^3}$ [−]							
		DB-2025 ($\theta_m = 0$)		DB-2025 ($\theta_m > 0$)		SF-2024		All	
		RMSLE	R^2	RMSLE	R^2	RMSLE	R^2	RMSLE	R^2
$\frac{q}{\sqrt{gH_{m0}^3}} = 0.12\exp\left(-1.72\frac{R_c}{H_{m0}\gamma_f\gamma_\beta}\right)$	(26)	0.74	0.46	0.84	0.38	0.96	0.46	0.87	0.47
$\frac{q}{\sqrt{gH_{m0}^3}} = 0.20\exp\left(-3.60\frac{R_c}{H_{m0}\gamma_f\gamma_\beta}s_{m-1,0}^{0.14}\right)$	(27)	0.51	0.74	0.58	0.70	0.65	0.75	0.60	0.75
$\frac{q}{\sqrt{gH_{m0}^3}} = 0.16\exp\left(-6.93\frac{R_c}{H_{m0}\gamma_f\gamma_\beta}s_{m-1,0,HF}^{0.36}\right)$	(28)	0.42	0.82	0.55	0.73	0.54	0.83	0.50	0.83
$\frac{q}{\sqrt{gH_{m0}^3}} = 0.16\exp\left(-6.93\frac{R_c}{H_{m0}\gamma_f}s_{m-1,0,HF}^{0.36}\right)$	(29)	0.42	0.82	0.94	0.22	0.54	0.83	0.58	0.76
$\frac{q}{\sqrt{gH_{m0}^3}} = 0.16\exp\left(-3.61\frac{R_c - 0.09H_{m0,LF}}{H_{m0}}\frac{1}{\gamma_f\gamma_\beta}s_{m-1,0}^{0.14}\right)$	(30)	0.51	0.74	0.56	0.72	0.63	0.77	0.58	0.76
$\frac{q}{\sqrt{gH_{m0}^3}} = 0.12\exp\left(-6.55\frac{R_c - 0.18H_{m0,LF}}{H_{m0}}\frac{1}{\gamma_f\gamma_\beta}s_{m-1,0,HF}^{0.36}\right)$	(31)	0.39	0.85	0.49	0.79	0.52	0.84	0.47	0.84
$\frac{q}{\sqrt{gH_{m0,HF}^3}} = 0.05\exp\left(-10.40\frac{R_c - 0.97H_{m0,LF}}{H_{m0,HF}}\frac{1}{\gamma_f\gamma_\beta}s_{m-1,0,HF}^{0.50}\right)$	(32)	0.36	0.88	0.56	0.74	0.52	0.86	0.45	0.87

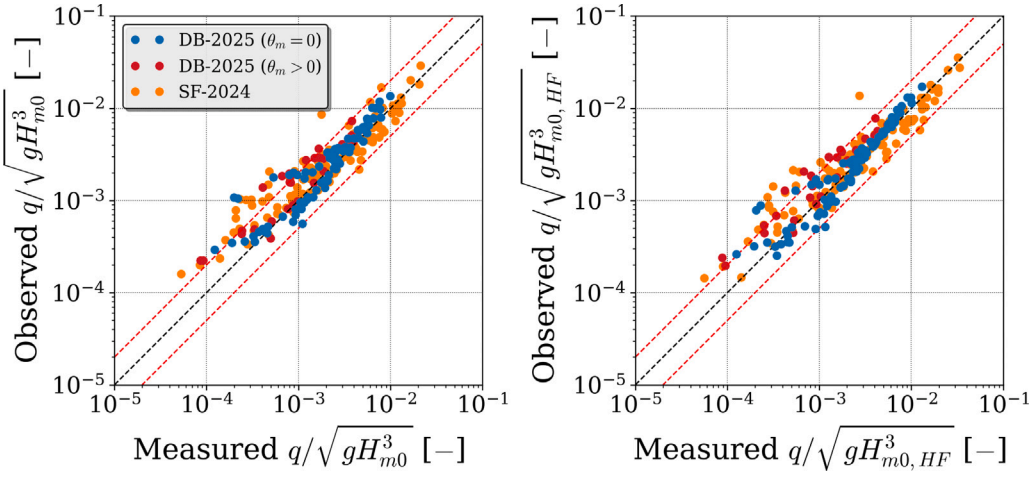

Fig. 18. Scatter plot Eq. (28) (left) and Eq. (32) (right) for the three subsets.

wave variables by only varying the wave direction. Both refraction, wave breaking, and nonlinear wave interactions will affect nearshore wave conditions. Therefore, the correction for these varying nearshore variables will result in a larger uncertainty that could be modeled with the approach in Mares-Nasarre (2025). Second, determining the nearshore wave direction is more difficult than in deep water, resulting in larger deviations in the mean direction. A third reason is the fact that it is difficult, or nearly impossible, if depth contours are parallel to the structure to obtain large wave directions ($\theta_m > 30°$) in shallow water because of refraction. Thus, it is difficult to estimate the asymptote for large wave directions, making it harder to detect a trend. Nevertheless, the current result shows that for $\theta_m < 30°$, the existing formulations seem valid.

The new proposed formulation can be applied to efficiently design a coastal structure in shallow water. As the directional spreading is not required, the methods to obtain the input parameters are not that restrictive. Analytical or empirical formulations, or numerical models can be applied to obtain the nearshore wave parameters. For example when Eq. (24) is used to estimate $H_{m0,LF}$ and applied in Eq. (32), the R^2 reduces to 0.84 for the combined dataset showing that the accumulated error is not very significant. For practitioners, it is recommended to use a numerical model to simulate the wave propagation over the foreshore and to compute the required wave parameters ($H_{m0,LF}$, $H_{m0,HF}$ and $T_{m-1,0,HF}$) from the nearshore wave spectrum.

8. Conclusions and recommendations

Physical model experiments are carried out in a wave basin to investigate the influence of directional spreading on the non-dimensional wave overtopping discharge, q^*, at rubble mound structures in shallow water. The effect of directional spreading is quantified by systematically varying wave height, wave steepness, directional spreading, and water depth. Additionally, tests with oblique wave conditions are conducted to study the effects of wave direction under shallow water conditions.

Hydrodynamic results show that wave parameters do not show significant variation when varying the directional spreading, except for the low-frequency wave energy. The directional spreading decreases due to refraction over the foreshore for the conditions with an offshore directional spreading larger than 10°, but increases again in the surfzone for most conditions.

Results show that nearshore low-frequency wave height ($H_{m0,LF}$) after the shoaling zone is strongly influenced by directional spreading, consistent with previous research. A new expression (Eq. (25) in Table

8) is proposed to predict the ratio of $H_{m0,LF}$ to total wave height based on relative water depth, offshore wave steepness, and offshore directional spreading, achieving an R^2 of 0.91. Excluding directional spreading from the formulation decreases the R^2 to 0.38, showing its importance.

The indirect influence of directional spreading on the individual overtopping volumes in shallow water through its effect on low-frequency wave energy is evident. The short waves on top of a low-frequency crest result in larger overtopping volumes than the short waves in the trough with a net increasing effect. This behavior is reflected in q^*, which shows a dependency on $H_{m0,LF}$, in addition to the relative crest level and short-wave steepness.

The existing formulations generally capture wave conditions with directional spreading reasonably well, with the best performance achieved by the expression proposed in De Ridder et al. (2024), which yields an RMSLE of 0.63. In contrast, the formulation that explicitly accounts for directional spreading shows a higher RMSLE of 1.40. This discrepancy arises because directional spreading itself does not significantly influence wave overtopping, but mainly its influence on low-frequency waves affects wave overtopping in shallow water.

The effect of oblique wave directions in shallow water appears similar to that observed in deep water. Therefore, the existing formulation by van Gent and van der Werf (2019) are recommended for application in shallow water conditions as well.

Coefficients of Equation 26 in De Ridder et al. (2024) are slightly revised using this new dataset, which better isolates the effect of low-frequency waves as the correlation between short-wave steepness and low-frequency height is lower due to imposed variations in directional spreading. The revised equations are validated against long-crested flume tests and new datasets with both short- and long-crested conditions and also with oblique attack. The expression including the low-frequency wave height results in the highest accuracy ($R^2 = 0.87$, Eq. (32)), while the expression with only the relative crest and short-wave steepness also performs accurately ($R^2 = 0.83$, Eq. (28)). The former formulation is preferred when reliable low-frequency wave height data are unavailable, whereas Eq. (32) is recommended when low-frequency waves can be determined accurately. When Eq. (25) is used as estimation for $H_{m0,LF}$ for Eq. (32), the R^2 reduced to 0.84.

The derived expressions (Eqs. (28) and (32)) are considered valid for shallow water conditions with $1.41 < h/H_{m0} < 2.15$, thus not for deep water conditions at the toe and not for extremely shallow water where overtopping is caused by the low-frequency waves rather than the short waves.

Because empirical formulations combine all processes into a single expression, it is recommended to validate numerical models for shallow-water conditions and to use these models when more detailed predictions are needed.

CRediT authorship contribution statement

Menno P. de Ridder: Writing – original draft, Visualization, Formal analysis, Data curation. **Dennis C.P. van Kester:** Writing – review & editing, Supervision. **Patricia Mares-Nasarre:** Writing – review & editing, Supervision. **Marcel R.A. van Gent:** Writing – review & editing, Supervision, Project administration, Funding acquisition.

Declaration of competing interest

The authors declare that they have no known competing financial interests or personal relationships that could have appeared to influence the work reported in this paper.

Acknowledgments

This study was conducted with the support of a TKI (Top Consortia for Knowledge and Innovation) subsidy (Delta Technology project CLIMACS-3D, project DEL191), the support by the 'Vereniging van Waterbouwers', and the Deltares Strategic Research Programme 'Moonshot 5'. We gratefully acknowledge the participation of Van Oord and The Weather Makers in the TKI project. The assistance by our colleagues Mr. Wesley Stet and Mr Peter Alberts, during the actual model testing is highly appreciated. Co-author Marcel R.A. van Gent is Editor-in-Chief of Coastal Engineering. The manuscript has been handled by one of the associate editors, who selected the reviewers and evaluated the manuscript without any influence on these decisions by the Editor-in-Chief.

Appendix A. Wave overtopping formulations

The formulation as proposed by De Ridder et al. (2024) with only wave steepness and wave height is (their Eq. (24)),

$$\frac{q}{\sqrt{gH_{m0}^3}} = 1.27\exp\left(-5.05\frac{R_c}{H_{m0}\gamma_f}s_{m-1,0}^{0.12}\right) \tag{A.1}$$

and with $s_{m-1,0,HF}$, H_{m0}, and $H_{m0,LF}$ is (Their Eq. (26)),

$$\frac{q}{\sqrt{gH_{m0}^3}} = 0.50\exp\left(-7.91\frac{R_c - 0.21H_{m0,LF}}{H_{m0}\gamma_f}s_{m-1,0,HF}^{0.30}\right) \tag{A.2}$$

Altomare et al. (2016) also performed experiments with extremely shallow foreshores with a foreshore slope of 1:35 and 1:50. Based on these results, they used Eq. (7) by including an equivalent slope (δ) concept in the breaker parameter instead of the actual slope(α) where this equivalent slope is given by,

$$\tanh\delta = \frac{1.5H_{m0} + R_{u2\%}}{(1.5H_{m0} - h)\cot m + (h + R_{u2\%})\cot\alpha} \tag{A.3}$$

where m is the foreshore slope and $R_{u2\%}$ is the wave run-up level exceeded by 2% of the incident waves given by,

$$\frac{R_{u2\%}}{H_{m0}} = \left(4 - \frac{1.5}{\sqrt{\xi_{m-1,0}}}\right) \tag{A.4}$$

As the breaker parameter is related to the $R_{u2\%}$, the solution has to be found iteratively.

Appendix B. Second-order steering

Because low-frequency waves strongly influence overtopping discharges, it is essential to generate them accurately in the basin. To

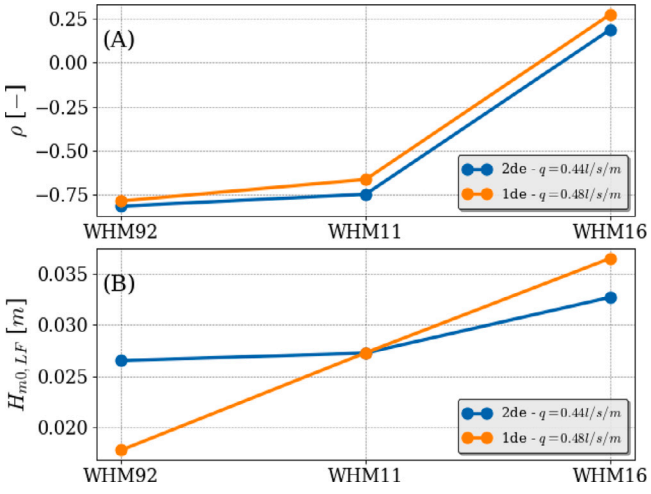

Fig. B.19. Correlation between short-wave groups and low-frequency waves (ρ, Panel A) and low-frequency wave height ($H_{m0,LF}$, Panel B) for three locations in the basin.

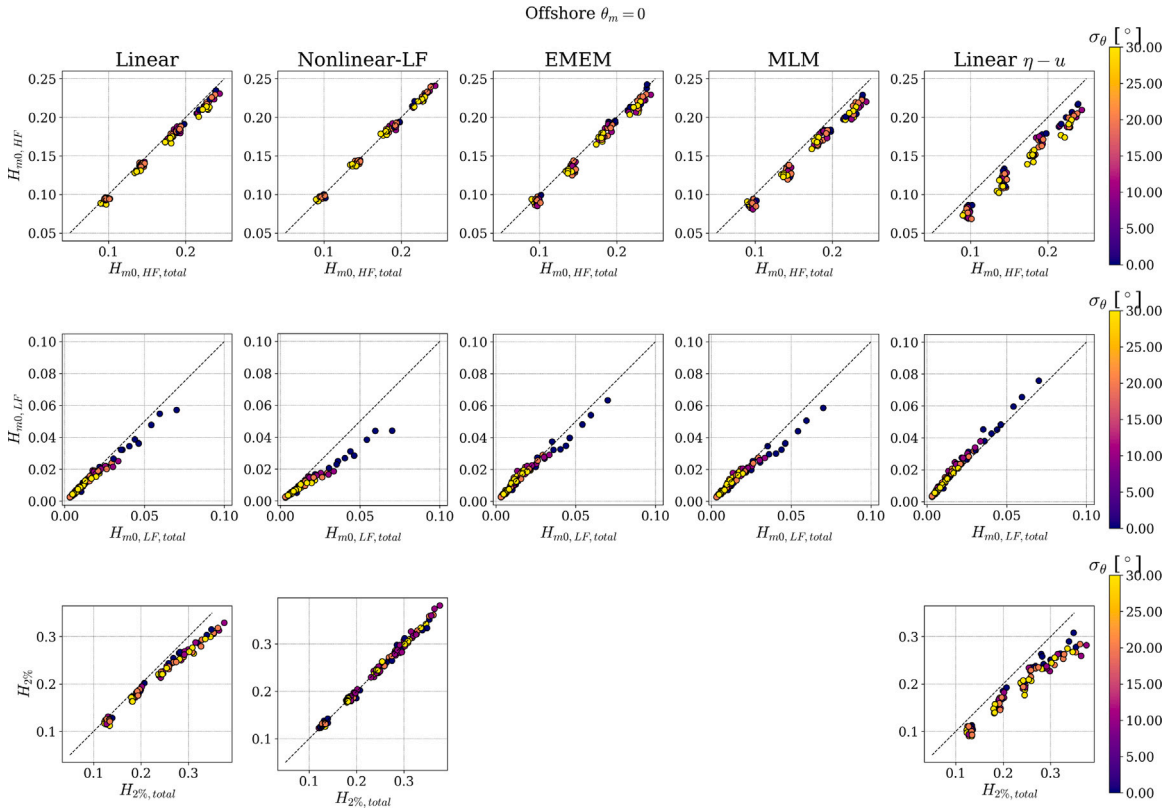

Fig. C.20. Comparison of the measured wave parameters ($H_{m0,HF}$, $H_{m0,LF}$ and $H_{2\%}$) and the incident wave parameter for several decomposition methods (columns) in deep water.

verify this, the results from a test with first- and second-order steering are compared. Fig. B.19 shows the correlation between short-wave groups and low-frequency waves (Panel A) and the low-frequency wave height (Panel B) at three locations. The second-order tests produce higher low-frequency wave heights offshore, showing that spurious waves are absent, and lower low-frequency wave heights nearshore, where only the bound wave exists. This is reflected in the slightly more negative correlation coefficient for the second-order steering suggesting that the generation correctly minimize the spurious wave.

Appendix C. Analyze methods

A comparison of several decomposition methods in both deep and shallow water for relevant wave parameters is shown in Figs. C.20 and C.21.

Appendix D. Refraction oblique waves

Fig. D.22 illustrates refraction for tests with oblique waves, comparing deep-water conditions (GRSM01) with two shallow water locations: EMS03 (mid-foreshore) and EMS06 (at the foreshore end). Panel A shows the refraction ratio ($\sin\theta_1 / \sin\theta_0$) as a function of the wave celerity ratio, where celerity is computed as $c = \omega_p / k_p$ with k_p obtained from the dispersion relation. Panel B presents the absolute wave directions, with the 1:1 line representing Snell's law based on the linear dispersion relation. Although the match is not perfect, the overall trend is consistent with theoretical expectations. Nearshore wave directions vary between 20° and 30° (squares in Panel B). The considerable scatter observed is attributed to uncertainty in the cross-spectral analysis, particularly in shallow water.

Appendix E. Effect foreshore

To illustrate the combined influence of the foreshore and the structure on mean wave overtopping, Fig. E.23 presents q^* as a function of R_c^*, computed using deep-water variables. Panel A shows the effect of wave steepness ($s_{m-1,0,deep}$), Panel B shows the directional spreading ($\sigma_{\theta,0}$), Panel C illustrates non-dimensional water depth (based on $H_{m0,deep}$ and h), and Panel D displays wave direction ($\theta_{m,0}$). Variations in wave steepness result in changes in q^* by a factor of 10 or more, highlighting its relevance. Directional spreading also affects overtopping, though to a lesser extent, with variations on the order of a factor of 1 to 5. Water depth exerts a significant influence as well, producing differences of approximately a factor of 10.

Appendix F. Effect directional spreading on mean overtopping discharge

The effect of σ_θ is implicitly represented through variations in $H_{m0,LF}$. Nevertheless, directional spreading itself may also directly influence wave overtopping. In Fig. F.24, values of q^* for long-crested waves are compared with those obtained under the corresponding short-crested conditions, for both deep and shallow water. It is hypothesized that, in shallow water, the influence of $H_{m0,LF}$ is dominant, whereas this effect is less pronounced in deeper water.

A further distinction can be made between offshore directional spreading (only valid for this particular foreshore), as applied by Altomare et al. (2020), and nearshore directional spreading. The influence factor proposed by Altomare et al. (2020) aligns reasonably well with the present dataset (Panels B and D). However, a clearer trend emerges when nearshore directional spreading is used, particularly in shallow water (Panel C). This trend, however, mainly reflects variations

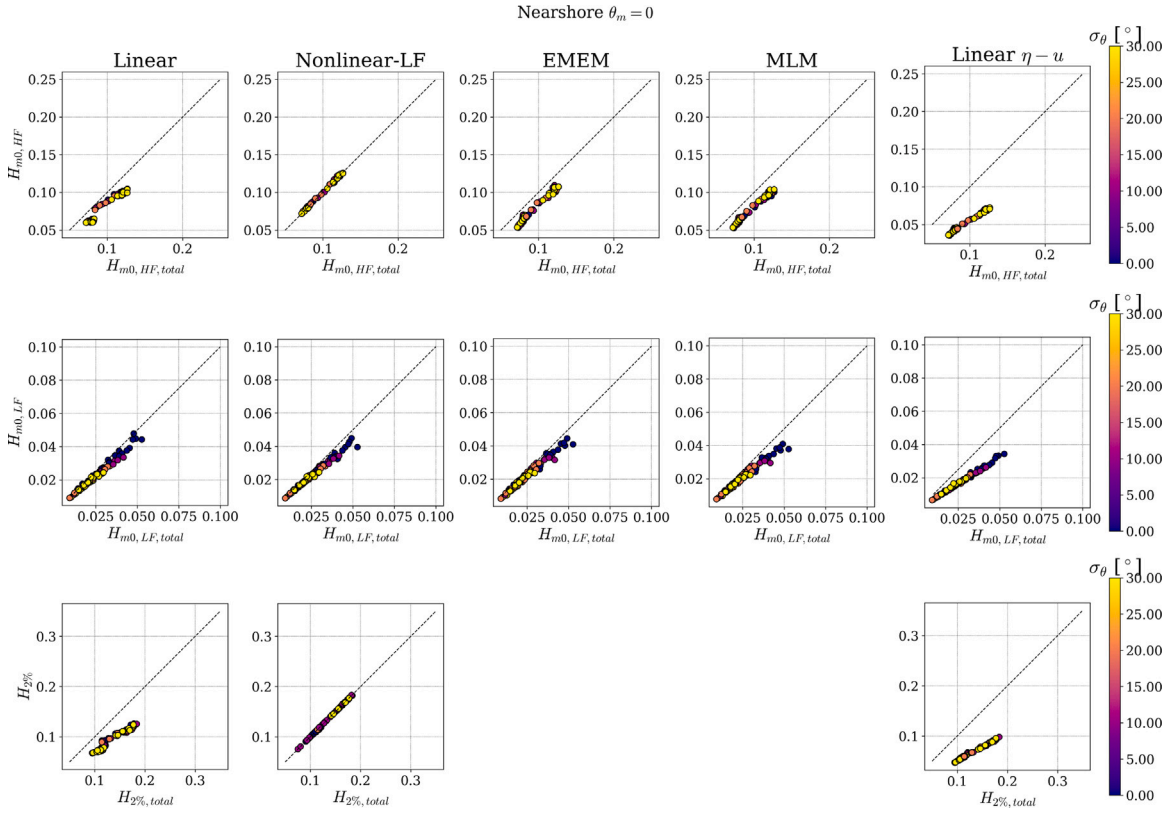

Fig. C.21. Comparison of the measured wave parameters ($H_{m0,HF}$, $H_{m0,LF}$ and $H_{2\%}$) and the incident wave parameter for several decomposition methods (columns) in shallow water.

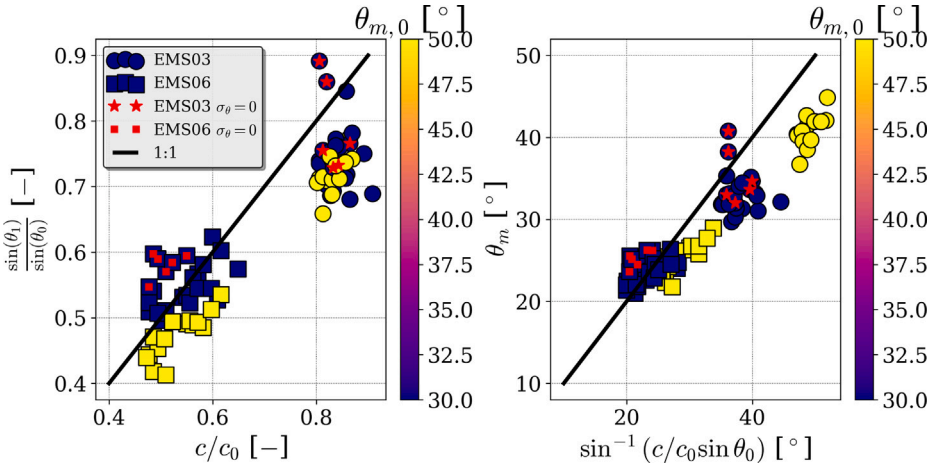

Fig. D.22. Refraction of tests with oblique waves with left the refraction value ($\sin\theta_1 / \sin\theta_0$) as a function of the celerity ratio and right the absolute direction as a function of Snell's law. The colors of the points show the offshore target direction.

in $H_{m0,LF}$, making it impossible to isolate the effect of directional spreading alone.

Two factors contribute to this limitation. First, in deep water (Panel A), the number of data points is small and the scatter is large. Second, in shallow water, low-frequency wave energy also varies, further complicating the separation of the directional-spreading effect from changes in $H_{m0,LF}$.

Appendix G. Confidence intervals for the parameters

For the proposed expression the confidence intervals of the fitted parameters are determined with the bootstrap technique. The proposed expressions have the following form:

$$q^* = p_1 \exp\left(p_2 \frac{R_c}{H_{m0}\gamma_f} s_{m-1,0,HF}^{p_3}\right) \tag{G.1}$$

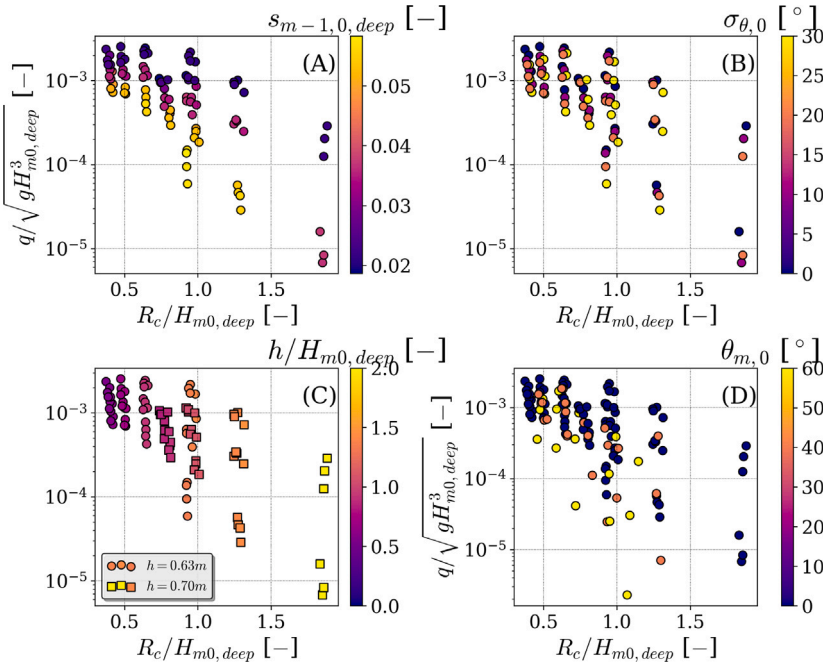

Fig. E.23. Non-dimensional mean overtopping discharge as function of the relative crest height for various wave parameters all based on the deep water value.

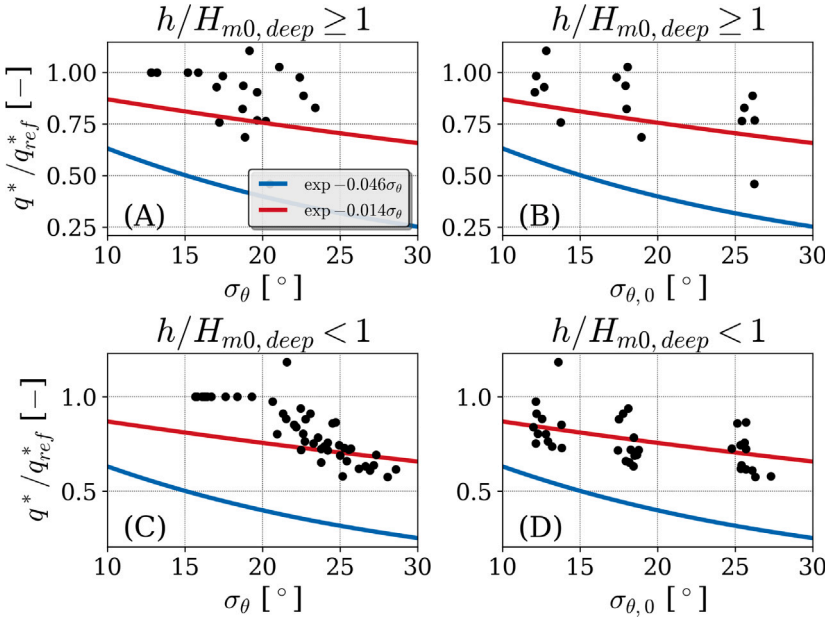

Fig. F.24. Ratio of q^* for long-crested waves to q^* for the corresponding short-crested waves, shown as a function of offshore directional spreading (Panels B and D) and nearshore directional spreading (Panels A and C). Panels A and B present the deep-water results, while Panels C and D show the shallow-water results. The directional-spreading formulations proposed by Altomare et al. (2020) are included for comparison.

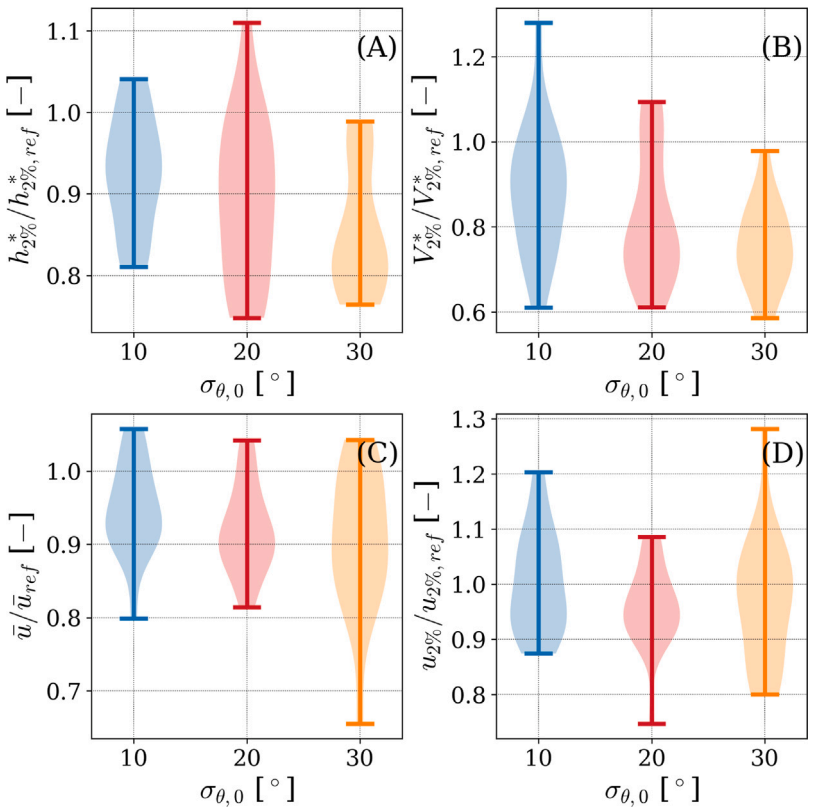

Fig. H.25. Violin plots for the non-dimensional 2% exceedance water-layer thickness (Panel A, $h^*_{2\%} = h_{2\%}/H_{m0}$), non-dimensional 2% exceedance individual overtopping volume (Panel B, $V^*_{2\%} = V_{2\%}/H^2_{m0}$), mean front velocity (Panel C, $\bar{u}$), and 2% exceedance front velocity (Panel D, $u_{2\%}$), compared to the results for zero directional spreading. Only tests with more than 50 overtopping events are shown.

Table G.9
95% confidence interval for the parameters in Eqs. (28), and (32).

Equation		p_1	p_2	p_3	p_4
Eq. (28)	5%	0.12	−7.75	0.32	–
	95%	0.22	−5.97	0.41	–
Eq. (32)	5%	0.04	−12.58	0.86	0.40
	95%	0.07	−7.91	1.13	0.59

or,

$$q^* = p_1 \exp\left(p_2 \frac{R_c - p_3 H_{m0,LF}}{H_{m0}} \frac{1}{\gamma_f} s^{p_4}_{m-1,0,HF}\right) \tag{G.2}$$

with parameters p_1, p_2, p_3 and p_4. Given these parameters the 95% confidence interval of these expressions are shown in Table G.9 presenting the spread of the parameter.

Appendix H. Wave overtopping individual events

The influence of $\sigma_{\theta,0}$ on $h_{2\%}$, $V_{2\%}$, $\bar{u}$, and $u_{2\%}$ is shown in Fig. H.25. The variables $h_{2\%}$ and $V_{2\%}$ were normalized, whereas the velocities were not. This is because velocity normalization with $\sqrt{gh}$ is typically applied, and $\sqrt{gh}$ remains constant for the different values of $\sigma_{\theta,0}$.

The results indicate that both $h_{2\%}$ and $V_{2\%}$ depend on $\sigma_{\theta,0}$, showing decreasing mean values for larger $\theta_{m,0}$. In contrast, $\bar{u}$ and $u_{2\%}$ show no substantial dependency on $\sigma_{\theta,0}$.

The findings in Fig. 16 are also confirmed for the 2% exceedance water-layer thickness in Fig. H.26. Similar behavior is observed for $h_{2\%}$, with the highest R^2 occurring when the normalization includes $H_{m0,LF}$, $s_{m-1,0,HF}$, and $H_{m0,HF}$, using the same coefficients as applied for q^* (Panel D). Furthermore, when $H_{m0,LF}$ is excluded, the influence of $H_{m0,LF}$ becomes evident: cases with substantial $H_{m0,LF}$ exhibit larger $h_{2\%}/H_{m0}$, demonstrating that the effect of $\sigma_{\theta,0}$ on $h_{2\%}$ also occurs through $H_{m0,LF}$ (Panel C). Similar trends were found for $V_{2\%}/H^2_{m0}$.

Glossary

α	Structure slope [−].
γ_f	Roughness factor [−].
γ_β	Influence factor for oblique waves [−].
η_{LF}	Low-pass band filtered time series [m].
$\langle\eta\rangle$	Wave setup [m].
$\xi_{m-1,0}$	Iribarren number of structure slope based on H_{m0} and $T_{m-1,0}$ [−] ($\frac{\tan\alpha}{\sqrt{2\pi H_{m0}/(gT^2_{m-1,0})}}$).
θ	Wave direction [°].
θ_m	Mean wave direction [°].
$\theta_{m,0}$	Offshore mean wave direction [°].
$\rho_{\eta_{LF}A}$	Correlation between low-frequency signal and short-wave envelope [−].
σ_θ	Directional spreading [°].
$\sigma_{\theta,0}$	Offshore directional spreading [°].
A	Short-wave group envelope [m].
c	Wave celerity [m/s].
D_{n50}	Nominal stone diameter (50th quantile of the stone size distribution) [m].
f	Frequency [Hz].
f_{cutoff}	Cutoff frequency [Hz].
h	Water depth [m].
$h_{2\%}$	2% exceedance water layer thickness in terms of incident waves.
$H_{2\%}$	Incident 2% exceedance wave height at the toe of the structure [m].
h_{crest}	Crest level with respect to the flume floor [m].
h_i	Individual water layer thickness [m].
H_{m0}	Incident significant wave height [m].
h_{deep}	Offshore water depth [m].

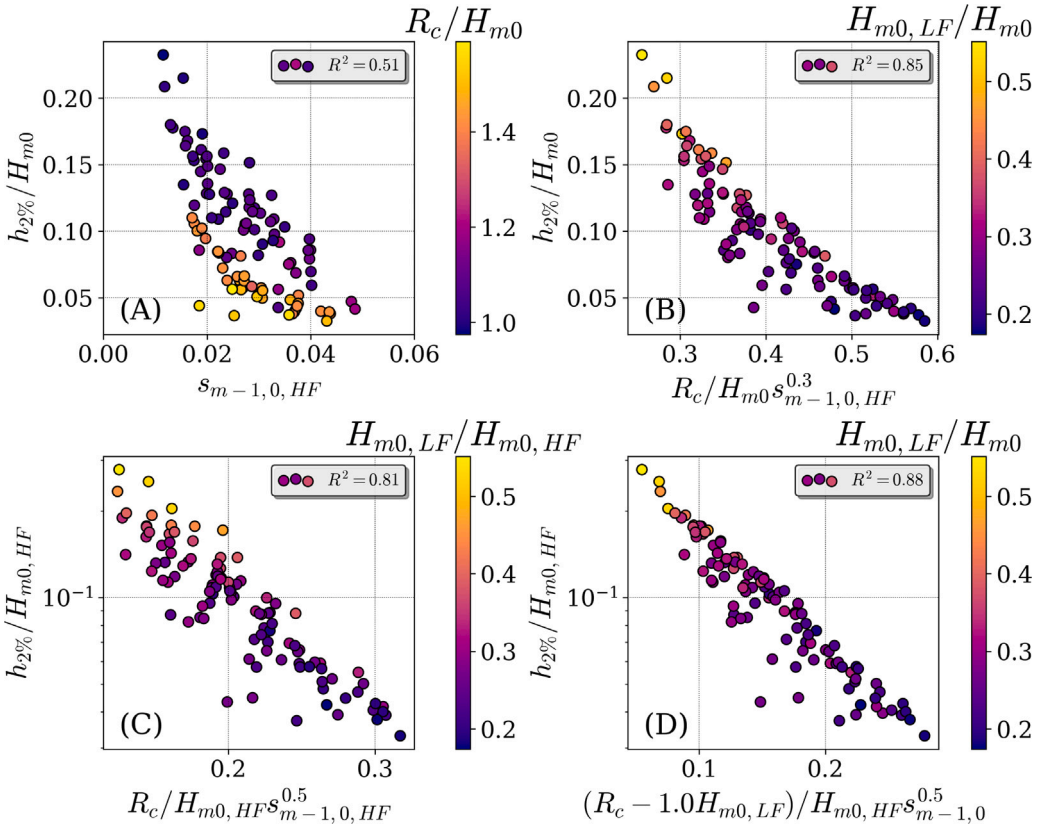

Fig. H.26. $h_{2\%}/H_{m0}$ as a function of $s_{m-1,0,HF}$ (Panel A), $R_c/(H_{m0}s^{0.3}_{m-1,0})$ (Panel B), $R_c/(H_{m0,HF}s^{0.5}_{m-1,0})$ (Panel C), and $(R_c - H_{m0,LF})/(H_{m0,HF}s^{0.5}_{m-1,0})$ (Panel D).

$H_{m0,deep}$	Offshore incident significant wave height [m].
$H_{m0,HF}$	Incident high-frequency wave height based on a cutoff-frequency at the toe of the structure [m].
$H_{m0,LF}$	Incident low-frequency wave height based on a cutoff-frequency at the toe of the structure [m].
k	Wave number associated to $T_{m-1,0}$ and h, through the dispersion relation [rad/m].
m	Tangent of foreshore slope [−].
P_{ov}	Number of overtopping waves divided by the total number of waves [−].
q	Mean overtopping discharge [m^3/s/m].
q^*	Non-dimensional mean overtopping discharge [−].
R_c	Crest height above still water level (Freeboard) [m].
R_c^*	Non-dimensional relative crest height [−] (R_c/H_{m0}).
$R_{u2\%}$	2% exceedance runup level [m].
s	Power in the 2-cosine directional spreading function [−].
$s_{m-1,0}$	Wave steepness based on the H_{m0} and $T_{m-1,0}$ [−] ($2\pi\frac{H_{m0}}{gT^2_{m-1,0}}$).
$s_{m-1,0,deep}$	Offshore wave steepness based on the $H_{m0,deep}$ and $T_{m-1,0,deep}$ [−] ($2\pi\frac{H_{m0,deep}}{gT^2_{m-1,0,deep}}$).
$s_{m-1,0,HF}$	Wave steepness based on the $H_{m0,HF}$ and $T_{m-1,0,HF}$ [−] ($2\pi\frac{H_{m0,HF}}{gT^2_{m-1,0,HF}}$).
$T_{m-1,0}$	Incident spectral period at the structure's toe [s].
$T_{m-1,0,HF}$	Incident spectral period of the short waves at the structure's toe [s].
u_i	Individual front velocity [m/s].
$u_{2\%}$	2 % exceedance front velocity [m/s].
V_i	Individual overtopping volume [m^3/m].
$V_{2\%}$	2 % exceedance individual overtopping volume [m^3/m].

Data availability

Data will be made available on request. The proposed formulations are available as Python functions at the Coastal Structures Toolbox: https://deltares-coastal-structures-toolbox.readthedocs.io/en/stable/.

References

Altomare, C., Suzuki, T., Chen, X., Verwaest, T., Kortenhaus, A., 2016. Wave overtopping of sea dikes with very shallow foreshores. Coast. Eng. 116, 236–257. http://dx.doi.org/10.1016/j.coastaleng.2016.07.002.

Altomare, C., Suzuki, T., Verwaest, T., 2020. Influence of directional spreading on wave overtopping of sea dikes with gentle and shallow foreshores. Coast. Eng. 157, 103654. http://dx.doi.org/10.1016/j.coastaleng.2020.103654.

Battjes, J.A., 1972. Golfoploop en golfoverslag. URL http://resolver.tudelft.nl/uuid:522060cb-8202-4276-bc48-ace65e137f40.

Battjes, J.A., 1974. Computation of Set-Up, Longshore Currents, Run-Up and Overtopping Due to Wind-Generated Waves (Ph.D. thesis). Delft university of technology, URL http://resolver.tudelft.nl/uuid:e126e043-a858-4e58-b4c7-8a7bc5be1a44.

Battjes, J.A., Groenendijk, H.W., 2000. Wave height distributions on shallow foreshores. Coast. Eng. 40 (3), 161–182. http://dx.doi.org/10.1016/S0378-3839(00)00007-7.

Capon, J., Greenfield, R., Kolker, R., 1967. Multidimensional maximum-likelihood processing of a large aperture seismic array. Proc. IEEE 55 (2), 192–211. http://dx.doi.org/10.1109/PROC.1967.5439.

Chen, W., Warmink, J.J., Van Gent, M.R.A., Hulscher, S.J.M.H., 2022. Numerical investigation of the effects of roughness, a berm and oblique waves on wave overtopping processes at dikes. Appl. Ocean Res. 118, 102971. http://dx.doi.org/10.1016/j.apor.2021.102971.

De Ridder, M.P., van Kester, D.C., Mares-Nasarre, P., Van Gent, M.R.A., 2025. Individual overtopping volumes, water layer thickness and front velocities at rubble mound breakwaters with a smooth crest in shallow water. Coast. Eng. 198, 104701. http://dx.doi.org/10.1016/j.coastaleng.2025.104701.

De Ridder, M.P., Kramer, J., Den Bieman, J.P., Wenneker, I., 2023. Validation and practical application of nonlinear wave decomposition methods for irregular waves. Coast. Eng. 183, 104311. http://dx.doi.org/10.1016/j.coastaleng.2023.104311.

De Ridder, M.P., Van Kester, D.C.P., Van Bentem, R., Teng, D.Y.Y., Van Gent, M.R.A., 2024. Wave overtopping discharges at rubble mound structures in shallow water. Coast. Eng. 194, 104626. http://dx.doi.org/10.1016/j.coastaleng.2024.104626.

Den Bieman, J.P., Van Gent, M.R.A., Van den Boogaard, H.F.P., 2021. Wave overtopping predictions using an advanced machine learning technique. Coast. Eng. 166, 103830. http://dx.doi.org/10.1016/j.coastaleng.2020.103830.

Eldrup, R.M., Lykke Andersen, T., 2019. Estimation of incident and reflected wave trains in highly nonlinear two-dimensional irregular waves. J. Waterw. Port Coast. Ocean. Eng. 145 (1), 04018038. http://dx.doi.org/10.1061/(ASCE)WW.1943-5460.0000497.

EurOtop, 2007. In: Pullen, T., Allsop, N.W.H., Bruce, T., Kortenhaus, A., Schüttrumpf, H., Van der Meer, J.W. (Eds.), EurOtop, European Overtopping Manual-Wave Overtopping of Sea Defences and Related Structures: Assessment Manual. Envrionment Agency, ENW, KFKI, URL http://www.overtopping-manual.com.

EurOtop, 2018. In: Van der Meer, J.W., Allsop, N.W.H., Bruce, T., De Rouck, J., Kortenhaus, A., Pullen, T., Schüttrumpf, H., Troch, P., Zanuttigh, B. (Eds.), Manual on Wave Overtopping of Sea Defences and Related Structures. URL www.overtopping-manual.com.

Forristall, G.Z., Ewans, K.C., 1998. Worldwide measurements of directional wave spreading. J. Atmos. Ocean. Technol. 15 (2), 440–469. http://dx.doi.org/10.1175/1520-0426(1998)015<0440:WMODWS>2.0.CO;2.

Goda, Y., 2009. Derivation of unified wave overtopping formulas for seawalls with smooth, impermeable surfaces based on selected CLASH datasets. Coast. Eng. 56 (4), 385–399. http://dx.doi.org/10.1016/j.coastaleng.2008.09.007.

Goda, Y., Kishara, Y., Kamiyama, Y., 1975. Laboratory investigation on the overtopping rate of seawalls by irregular waves. URL http://resolver.tudelft.nl/uuid:26a7a1aa-16ce-4468-8da2-68589dcfd090.

Guza, R.T., Feddersen, F., 2012. Effect of wave frequency and directional spread on shoreline runup. Geophys. Res. Lett. 39 (11), http://dx.doi.org/10.1029/2012GL051959.

Guza, R., Thornton, E., Holman, R., 1984. Swash on steep and shallow beaches. Coast. Eng. Proc. (19), 48. http://dx.doi.org/10.9753/icce.v19.48.

Hashimoto, N., Nagai, T., Asai, T., 1995. Extension of the maximum entropy principle method for directional wave spectrum estimation. In: Coastal Engineering 1994. Vol. 57, 232–246. http://dx.doi.org/10.1061/9780784400890.019.

Hasselmann, D.E., Dunckel, M., Ewing, J.A., 1980. Directional wave spectra observed during JONSWAP 1973. J. Phys. Oceanogr. 10 (8), 1264–1280. http://dx.doi.org/10.1175/1520-0485(1980)010<1264:DWSODJ>2.0.CO;2.

Henderson, S.M., Guza, R.T., Elgar, S., Herbers, T.H.C., Bowen, A.J., 2006. Nonlinear generation and loss of infragravity wave energy. J. Geophys. Res.: Ocean. 111 (C12), http://dx.doi.org/10.1029/2006JC003539.

Herbers, T.H.C., Burton, M.C., 1997. Nonlinear shoaling of directionally spread waves on a beach. J. Geophys. Res.: Ocean. 102 (C9), 21101–21114. http://dx.doi.org/10.1029/97JC01581.

Herbers, T.H.C., Elgar, S., Guza, R.T., 1999. Directional spreading of waves in the nearshore. J. Geophys. Res.: Ocean. 104 (C4), 7683–7693. http://dx.doi.org/10.1029/1998JC900092.

Holthuijsen, L.H., 2007. Waves in Oceanic and Coastal Waters. Cambridge University Press, http://dx.doi.org/10.1017/CBO9780511618536.

Irías Mata, M., Van Gent, M.R.A., 2023. Numerical modelling of wave overtopping discharges at rubble mound breakwaters using OpenFOAM®. Coast. Eng. 181, 104274. http://dx.doi.org/10.1016/j.coastaleng.2022.104274.

Isobe, M., Kondo, K., 1985. Method for estimating directional wave spectrum in incident and reflected wave field. In: Coastal Engineering 1984. American Society of Civil Engineers, pp. 467–483. http://dx.doi.org/10.1061/9780872624382.033.

Iversen, S.K., Eldrup, M.R., Lykke Andersen, T., Frigaard, P., 2025. The NL-SORS method for separation of nonlinear multidirectional waves into incident and reflected wave trains. Coast. Eng. 201, 104785. http://dx.doi.org/10.1016/j.coastaleng.2025.104785.

Janssen, T.T., Battjes, J.A., Van Dongeren, A.R., 2003. Long waves induced by short-wave groups over a sloping bottom. J. Geophys. Res.: Ocean. 108 (C8), http://dx.doi.org/10.1029/2002JC001515.

Kikkawa, H., Shi-igai, H., Kono, T., 1968. Fundamental study of wave over-topping on levees. Coast. Eng. Jpn. 11 (1), 107–115. http://dx.doi.org/10.1080/05785634.1968.11924074.

Klopman, G., Dingemans, M.W., 2001. Wave interactions in the coastal zone. In: Proc. 16th International Workshop on Water Waves and Floating Bodies.

Kuik, A.J., Van Vledder, G.P., Holthuijsen, L.H., 1988. A method for the routine analysis of Pitch-and-Roll Buoy Wave Data. J. Phys. Oceanogr. 18 (7), 1020–1034. http://dx.doi.org/10.1175/1520-0485(1988)018<1020:AMFTRA>2.0.CO;2.

Lashley, C.H., Jonkman, S.N., van der Meer, J., Bricker, J.D., Vuik, V., 2022. The influence of infragravity waves on the safety of coastal defences: a case study of the Dutch Wadden Sea. Nat. Hazards Earth Syst. Sci. 22 (1), 1–22. http://dx.doi.org/10.5194/nhess-22-1-2022.

Lashley, C.H., Van der Meer, J., Bricker, J.D., Altomare, C., Suzuki, T., Hirayama, K., 2021. Formulating wave overtopping at vertical and sloping structures with shallow foreshores using deep-water wave characteristics. J. Waterw. Port Coast. Ocean. Eng. 147 (6), 04021036. http://dx.doi.org/10.1061/(ASCE)WW.1943-5460.0000675.

Levenberg, K., 1944. A method for the solution of certain non-linear problems in least squares. Quart. Appl. Math. 2 (2), 164–168. http://dx.doi.org/10.1090/qam/10666.

Longuet-Higgins, M.S., 1963. Observation of the directional spectrum of sea waves using the motions of a floating buoy. Ocean Wave Spectra.

Mares-Nasarre, P., 2025. Probabilistic estimation of the mean wave overtopping discharge on mound breakwaters. Coast. Eng. 201, 104792. http://dx.doi.org/10.1016/j.coastaleng.2025.104792.

Mares-Nasarre, P., Molines, J., Gómez-Martín, M.E., Medina, J.R., 2021. Explicit neural network-derived formula for overtopping flow on mound breakwaters in depth-limited breaking wave conditions. Coast. Eng. 164, 103810. http://dx.doi.org/10.1016/j.coastaleng.2020.103810.

Marquardt, D.W., 1963. An algorithm for least-squares estimation of nonlinear parameters. J. Soc. Ind. Appl. Math. 11 (2), 431–441. http://dx.doi.org/10.1137/0111030.

Martins, K., Bonneton, P., Michallet, H., 2021. Dispersive characteristics of non-linear waves propagating and breaking over a mildly sloping laboratory beach. Coast. Eng. 167, 103917. http://dx.doi.org/10.1016/j.coastaleng.2021.103917.

Mitsuyasu, H., Tasai, F., Suhara, T., Mizuno, S., Ohkusu, M., Honda, T., Rikiishi, K., 1975. Observations of the directional spectrum of ocean WavesUsing a Clover-leaf Buoy. J. Phys. Oceanogr. 5 (4), 750–760. http://dx.doi.org/10.1175/1520-0485(1975)005<0750:OOTDSO>2.0.CO;2.

Nørgaard, J.Q.H., Lykke Andersen, T., Burcharth, H.F., Steendam, G.J., 2013. Analysis of overtopping flow on sea dikes in oblique and short-crested waves. Coast. Eng. 76, 43–54. http://dx.doi.org/10.1016/j.coastaleng.2013.01.012.

Owen, M.W., 1980. Design of Seawalls Allowing for Wave Overtopping, HR-Wallingford. Technical Report UK., and Technical Report EX-924.

Pearson, K., 1895. VII. Note on regression and inheritance in the case of two parents. Proc. R. Soc. Lond. 58 (347–352), 240–242. http://dx.doi.org/10.1098/rspl.1895.0041.

Saville, T., 1955. Laboratory Data on Wave Run-Up and Overtopping on Shore Structures, Vol. 64, US Beach Erosion Board.

Suzuki, T., Altomare, C., Verwaest, T., Trouw, K., Zijlema, M., 2014. Two-dimensional wave overtopping calculation over a dike in shallow foreshore by SWASH. In: Proceedings of the 34th International Conference on Coastal Engineering, Seoul, Korea. pp. 15–20.

TAW, 2002. Wave Run-Up and Wave Overtopping at Dikes. Technical Report, Technical Advisory Committee for flood defence in the Netherlands (TAW) Delft.

Thornton, E.B., Guza, R.T., 1982. Energy saturation and phase speeds measured on a natural beach. J. Geophys. Res.: Ocean. 87 (C12), 9499–9508. http://dx.doi.org/10.1029/JC087iC12p09499.

Van der Meer, J.W., Janssen, J.P.F.M., 1994. Wave Run-Up and Wave Overtopping at Dikes and Revetments, Delft Hydraulics, Publication No. 485. Delft Hydraulics, publication no. 485.

Van Gent, M.R.A., 1999. Physical model investigations on coastal structures with shallow foreshores: 2D model tests with single and double-peaked wave energy spectra. URL http://resolver.tudelft.nl/uuid:1b4729de-2e86-4b8a-98d5-48d8e07d5902.

Van Gent, M.R.A., 2001. Wave runup on dikes with shallow foreshores. J. Waterw. Port Coast. Ocean. Eng. 127 (5), 254–262. http://dx.doi.org/10.1061/(ASCE)0733-950X(2001)127:5(254).

Van Gent, M.R.A., 2019. Climate adaptation of coastal structures. In: Proceedings of the SCACR19 9th Short Course/Conference on Applied Coastal Research, Bari, Italy. pp. 9–11.

Van Gent, M.R.A., 2021. Influence of oblique wave attack on wave overtopping at caisson breakwaters with sea and swell conditions. Coast. Eng. 164, 103834. http://dx.doi.org/10.1016/j.coastaleng.2020.103834.

Van Gent, M.R.A., 2022. Wave Overtopping at Dikes and Breakwaters Under Oblique Wave Attack. Vol. 37, Coastal Engineering Research Council, p. 5. http://dx.doi.org/10.9753/icce.v37.papers.5.

Van Gent, M.R.A., Teng, D.Y.Y., 2023. Climate adaptation of coastal structures: Application of adaptation pathways for rubble mound breakwaters. In: Proc. PIANC-COPEDEC X, Manila.

Van Gent, M.R.A., Van Marrewijk, J., Mares-Nasarre, P., 2025. Guidelines on wave overtopping discharges at rubble mound breakwaters including slope angle effects. J. Coast. Hydraul. Struct. 5, http://dx.doi.org/10.59490/jchs.2025.0048.

van Gent, M.R., van der Werf, I.M., 2019. Influence of oblique wave attack on wave overtopping and forces on rubble mound breakwater crest walls. Coast. Eng. 151, 78–96. http://dx.doi.org/10.1016/j.coastaleng.2019.04.001.

Van Leeuwen, P.J., Klopman, G., 1996. A new method for the generation of second-order random waves. Ocean Eng. 23 (2), 167–192. http://dx.doi.org/10.1016/0029-8018(95)00027-5.

Victor, L., Van der Meer, J.W., Troch, P., 2012. Probability distribution of individual wave overtopping volumes for smooth impermeable steep slopes with low crest freeboards. Coast. Eng. 64, 87–101. http://dx.doi.org/10.1016/j.coastaleng.2012.01.003.

Wei, Z., Dalrymple, R.A., Xu, M., Garnier, R., Derakhti, M., 2017. Short-crested waves in the surf zone. J. Geophys. Res.: Ocean. 122 (5), 4143–4162. http://dx.doi.org/10.1002/2016JC012485.

Zelt, J., Skjelbreia, J.E., 1993. Estimating incident and reflected wave fields using an arbitrary number of wave gauges. In: Coastal Engineering 1992. American Society of Civil Engineers, pp. 777–789. http://dx.doi.org/10.1061/9780872629332.058.